University of Stavanger

FACULTY OF SCIENCE AND TECHNOLOGY

MASTER'S THESIS

Study program/specialization: Mechanical and Structural Engineering and Material Science Specialization: Mechanical Systems	Autumn, 2021 Open
Author: Abuzar Ghaffari	
	Author's signature
Program coordinator: Knut Erik Teigen Giljarhus Supervisor(s): Knut Erik Teigen Giljarhus	
Title of master's thesis: Optimization of blade profiles for a coaxial drone	
Credits: 30	
Keywords: UAV, Nordic Unmanned, CFD, Co-Axial rotor setup, Low Reynolds, Axial Separation	Number of pages: 51 Stavanger, 15/06/2021 date/month/year

Abstract

In the civil market, an increase in the demand for drone technology has given rise to rotor blade design. Much research has to undergo to enhance the efficiency of propellers. In this research, we want to improve the propeller design efficiency in term of flight endurance. The main goal is in the variation of axial separation by using computational fluid dynamics in OpenFOAM. We found that the variation of distance between two propellers has improved overall efficiency significantly during computational analysis. At the lowest separation, the interference disturbance created by the lower propeller affects the upper propeller performance by lowering total thrust. However, if we increase the distance, the lower propeller faces the downwash created by the upper propeller resulting in the efficiency loss of the lower one. One can increase or decrease the axial separation, but the overall efficiency would remain the same. Hence, it has been found that at 0.65z/R, we have the maximum efficiency.

Preface

This master thesis is written in collaboration with a company based in Sandnes, Nordic Unmanned AS, at the Department of Mechanical and Structural Engineering and Materials Science of the University of Stavanger (Uis), to qualify for the master's degree in Engineering Structures with specialization in Mechanical Systems.

First and foremost, I would like to express sincere gratitude to my University (UiS) supervisor for this thesis, Knut Erik Giljarhus (PhD). Knut Erik way of encouragement and support is amicable, especially in the challenging times of lockdown due to COVID-19. It was a great privilege and honour to work under his supervision.

I am also grateful to Jørgen Apeland, my external supervisor from Nordic Unmanned AS, to provide all the necessary information about the project. I would also like to thank the Kjell Vistnes Randaberg and Sondre Andersen Gysland bachelor group for their intriguing conversations and information to assist in leading me and validating my simulations.

Here, I also want to acknowledge the effort of Mr Theodor Ivesdal, who helped me to use the Uis lab cluster for my simulations. Finally, I would like to thank all my family and friends for encouraging and supporting me.

CONTENTS

Nomenclature

Acronyms

BEMT	Blade Element Momentum Theory
LSB	Laminar Separation Bubble
NACA	National Advisory Committee for Aeronautics
CFD	Computational Fluid Dynamics
CAD	Computer- Aided Design
PISO	Pressure Implicit with Splitting of Operator
OpenFOAM	Open-source Field Operations and Manipulations
RPM	Revolutions Per Minute
Re	Reynolds Number
RANS	Reynolds-Average Navier Stokes
SA	Spalart Allmaras
SIMPLE	Semi-Implicit Method for Pressure Linked Equations
UAV	Unmanned Aerial Vehicle
UiS	University of Stavanger

Other Symbols

A	Surface Area
ρ	Density
F_L	Lift Force
F_D	Drag Force
C_D	Drag Coefficient
C_L	Lift Coefficient
g	Gravitational Constant
Δs	First Layer Thickness
Γ	Diffusion coefficient
κ	Compressibility coefficient

μ	Dynamic viscosity
∂	Partial derivative
ϕ	Generic flux
τ	Shear Stress
μ_τ	Friction Velocity
c	Chord length
div	Divergence
$divU$	Volumetric deformation
$grad$	Gradient
k	Turbulent kinetic energy
L	Characteristic Length
l	Chord width
r	Radius
U	Mean velocity in the x-direction
u	Instantaneous velocity in the x-direction
$u\prime$	Fluctuation velocity in the x-direction
V	Mean velocity in the y-direction
v	Instantaneous velocity in the y-direction
$v\prime$	Fluctuation velocity in the y-direction
w	Instantaneous velocity in z-direction
$w\prime$	Fluctuation velocity in z-direction
y^+	Dimensionless quantity

1 Introduction

The rapidly increasing civil market has generated the requirement of Unmanned Aerial Vehicles (UAVs) [1], that can outperform traditional helicopter in many aspects. A UAV with minimal cost and high efficiency are designed for a particular job, such as photography, airborne inspection, 3D capturing of terrain, cinematography, and thermographic imaging [2], potentially faster and cheaper than a helicopter. Furthermore, the chance of fatalities has also been reduced due to the remote system.

Nordic Unmanned, keeping all the aspects in mind, has created a business to use these UAVs to benefit the civil market. These UAVs are designed depending upon the mission profile, such as some UAVs are used for farming, so they should carry more weight, some have a potential role in surveillance. Hence these required more endurance. Based on these requirements, they come in many shapes and sizes. However, in this thesis, we will optimize the load carry capacity of the drone by configuring the propeller blades. For this purpose, Staaker BG-200 with a carrying capacity of 25 kg will be used.

Most drone configuration has a coaxial propeller design known as an overlapping propulsion system that provides the smallest volume per thrust output [3]. However, there is a drawback to a coaxial configuration. The upper propeller outperforms the lower propeller due to the downwash generated by an upper propeller that decreases the efficiency of the lower rotor blade, which cause the combined thrust of the coaxial propeller to be lower than the single rotor system.

Unlike manned helicopters, UAVs operate low Reynolds Number. It becomes quite challenging to predict the flow properties due to boundary layer separation, and the transition region to turbulence is encountered at a low Reynolds Number. At Langley Research Center in Hampton, Walker studies show that Eppler 387 airfoil is dominated by Laminar Separation bubble at Reynolds Number below 2,00,000. To deal with that, the Spalart Allmaras turbulence model will be used for modelling in CFD due to its capability to deal with entirely high Reynolds Number turbulent flows. However, it demonstrates no re-laminarization [4]. Different research has been made to deal with the efficiency loss of the lower propeller, such as Leishman and Anathan found that if the diameter of the lower propeller is more significant than the upper propeller, we can reduce the efficiency loss by getting out the slipstream of the upper propeller.

Furthermore, through studies, it has been found that axial separation also affects the overall efficiency of coaxial configuration. By the studies of Brazinaskas et al. [3], we came to know that at an axial separation of 0.6 z/D, the upper propeller performs much better than a single rotor; however, if the separation is reduced to just 0.05 z/D, the upper propeller is at lowest efficiency, whereas D is the diameter of the rotor blade.

Keeping these drawbacks Nordic Unmanned requires us to design an optimized drone with the highest flight endurance. So, the previous coaxial configuration will be optimized with the new configuration of the coaxial propeller. Computational Fluid Dynamics will be used with the tool OpenFOAM a volume of fluid method. A propeller G28" x 9.2" will be used, and the combined efficiency of the propeller will be calculated at different axial separation. Then the most efficient will be selected, and flight endurance will be calculated. The theory about the method and equations are presented in chapter two, and chapter three has details on the numerical approach. Chapter four presents the details of the drone and propeller, while chapter five has the 2D simulation of airfoil used for validation of the model. In chapter six, the 3D model will be validated, and CFD results for coaxial configuration and flight endurance will be presented.

2 Theory

This section will discuss the Aerodynamics of an airfoil, following that the Reynolds Number will be discussed. Boundary layer and flow separation will also be addressed. Then the laminar separation bubble phenomenon will be demonstrated. Reynolds Averaging of turbulent parameters will be shown, and Spalart Allmaras turbulence model will be studied.

2.1 Aerodynamics

Aerodynamics is the science of how the air travels around objects. The laws of aerodynamics describe how an aircraft can fly. Aerodynamics affects anything that travels through the air. Aerodynamics affect a rocket blasting off the launch pad and a kite-flying into the sky. Aerodynamics also affects automobiles, as air flows around them. The lift provided by the plane must be greater than the gravitational forces pressing on the aircraft in order to maintain an object in the air.

Moreover, to propel a plane ahead, the forward thrust must be greater than the drag forces acting on it. When the form of an item forces the streamlines to curve around it, the lift is created. A pressure gradient is required to curve the streamlines.

As the velocity of the streamlines increases or the curve of the streamlines reduces, the pressure gradient acts as a centripetal force, increasing the pressure difference. This results in decreasing pressure on the airfoil's upper surface and increasing pressure on the bottom surface of the airfoil, assuming atmospheric pressure far from the airfoil. This pressure differential results in a total aerodynamic force, broken down into lift- and drag-force components.

The study of flight and science in the construction and operation of an aircraft, known as aeronautics, is based on aerodynamics. In order to design aircraft that fly through the atmosphere of this Earth, aviation technologists use the fundamentals of aerodynamics. The lifting and drag factors can affect the pressure gradient, shape, and size, affecting the rails' curvature [5]. The movement affects fluid density or velocity in the streamlines. Additional considerations for a propeller are propeller inflow and outflow, particularly for coaxial rotor installation where the lower propeller is operated on the upper propeller slipstream. A rotating wing can be seen as a propeller, and the factors affecting a propeller lift are the same as a wing. The wind speed changes

along the propeller's leading edge because of the rotational motion. At the same time, a plane wing has a wind speed equal to the aircraft speed. Wind speed refers, therefore, to the perpendicular wind striking at the leading edge of the wing. In contrast, wind speed refers to the perpendicular wind striking at the front edge of the propeller.

2.2 Drag and Lift

Drag is caused by the component of the resultant aerodynamic force that is parallel to the airflow. Lift is caused by the component of the resultant aerodynamic force that is perpendicular to airflow. Aerodynamic resultant force and moment occur due to two primary sources:

- Pressure distribution over the body surface
- Shear stress distribution over the body surface

The value of drag & lift at different speeds is determined from the apparatus. This is then used to derive the coefficient of drag and Lift.
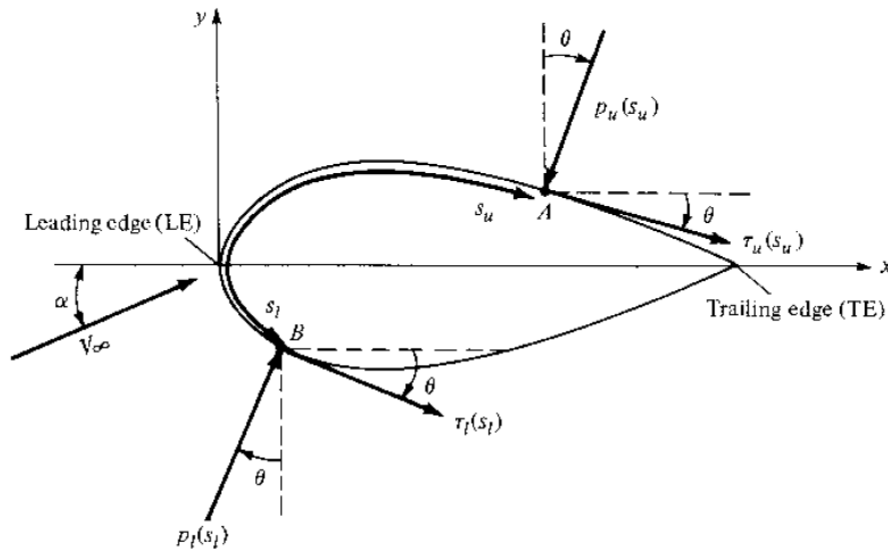

Figure 2.1 Pressure and shear stress distribution over a two-dimensional surface [5].

In figure 1:

- S_u Is the distance from the leading edge measured along the body surface to an arbitrary point A on the upper surface.
- S_l Is the distance to an arbitrary point B on the lower surface.

- P_u and τ_u denote the pressure and shear stress on the upper surface. Both P_u and τ_u are functions of S_u.

- p_l and τ_l are the corresponding quantities on the lower surface and are functions of S_l.

- At a given point, the pressure is normal to the surface and is oriented at an angle θ relative to the perpendicular.

- Shear stress is tangential to the surface and is oriented at the same angle θ relative to the horizontal.

The total normal and axial forces per unit span are obtained by integrating from the leading edge (LE) to the trailing edge (TE),

$$N' = -\int_{LE}^{TE}(p_u cos\theta + \tau_u sin\theta)ds_u + \int_{LE}^{TE}(p_l cos\theta - \tau_l sin\theta)ds_l$$

$$A' = -\int_{LE}^{TE}(-p_u sin\theta + \tau_u cos\theta)ds_u + \int_{LE}^{TE}(p_l sin\theta + \tau_l cos\theta)ds_l$$

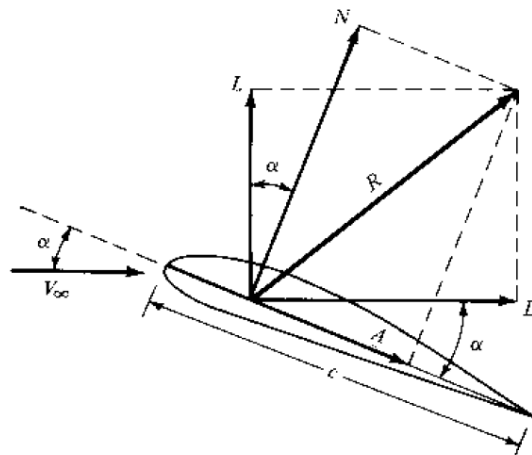Resultant aerodynamic force and its components

Figure 2.2 Components of velocity and forces across the airfoil [6].

2.2.1 Freestream Velocity

The flow far away from the body is called the freestream, and hence V∞ is also called the freestream velocity. The chord c is the linear distance from the leading edge to the trailing edge of

the body. Sometimes, R is split into components perpendicular and parallel to the chord, as shown in figure x.

L ≡ lift ≡ component of R perpendicular to V_∞

D ≡ drag ≡ component of R parallel to V_∞

N ≡ normal force ≡ component of R perpendicular to c

A ≡ axial force ≡ component of R parallel to c

2.2.2 Angle of Attack

The angle of attack α is defined as the angle between c and V∞. Hence, α is also the Angle between L and N and between D and A.

The geometrical relation between these two sets of components is:

$$L = N \cos \alpha - A \sin \alpha$$

$$D = N \sin \alpha + A \cos \alpha$$

Let ρ_∞ and V_∞ be the density and velocity, respectively, in the **freestream**, far ahead of the body.

We define a dimensional quantity called the freestream dynamic pressure as

$$q_\infty \equiv \frac{1}{2} \rho_\infty V_\infty^2$$

2.3 COEFFICIENT OF LIFT & DRAG

2.3.1 Lift Coefficient

The lift coefficient (C_L, C_N) is a dimensionless coefficient that relates the lift generated by a lifting body to the fluid density around the body, the fluid velocity, and an associated reference area. A lifting body is a foil or a complete foil-bearing body such as a fixed-wing aircraft.

$$C_L = \frac{L}{q_\infty s}$$

2.3.2 Drag Coefficient

A dimensionless quantity is used to quantify the **drag** or resistance of an object in a fluid environment, such as air or water. The **drag coefficient** is always associated with a particular surface area.

$$C_D = \frac{D}{q_\infty S}$$

The symbol in capital letters listed above (i.e., CD, CL) denotes the force coefficient for a complete three-dimensional body such as an aircraft or a finite wing.

Considering a propeller rotating in still air, the rotating propeller's influx in conjunction with the rotating wind velocity causes airflow in what is known as the relative rotational wind speed. The airflow above the rotating propeller is referred to in this thesis as the injection. Moreover, the outflow, which will extend the inflow after the propeller has been left. Slipstream is underneath the outflow propeller. Airstream is called induced flow in a negative Z- direction, affecting movement direction. Airstream Attack angle is achieved by inflow by the increased induced rate of flow, leading to a decline in the relative direction of the wind rotation, which usually decreases the angle of attack. Since the angle of attack and the close linked lift, a rise in the induced flow magnitude would reduce the lifting due to reducing the angle of attacks' new relative rotary wind orientation.

2.4 Co-axial

A coaxial propeller setup is a configuration in which a pair of propellers operate over each other. The two propellers create an elevation the same as an isolated propeller, but the resultant airflow differs depending on the interference between the bottom and top of the propeller. As indicated in the introduction, a coaxial propellor setup is advantageous to cancel the torque generated by a single rotor and remove the need for a vertical tail rotor. Apart from the influx generated by the bottom thrust in a coaxial setup, the lower thrust operates in the upper thrust.

2.5 Reynolds number

Turbulence entirely depends upon inertial and viscous forces. By increasing the inertial forces, the flow becomes turbulent, and by increasing viscous forces, turbulence effects decrease. We can

define this by a non-dimensional coefficient known as Reynolds **N**umber, which is the function of inertial and viscous forces.

$$Re = \frac{vl}{v}$$

The Reynolds Number shows the relationship between the inertial forces and viscous forces. With the increase in Reynolds Number, the inertial forces dominate the viscous forces, instability arises, and flow undergoes transition till it becomes fully turbulent. However, with large viscous forces, these instabilities are died out. Hence flow remains laminar. In our case, the airfoil is ideally represented the flat plate case. In which boundary layer is generated due to no-slip condition. If the Reynolds Number is below the critical value, its boundary layer remains stable. However, if the Reynold Number increases till critical value, $Re_{crit} = 1 \times 10^5$, boundary layer will face the transition process and become fully turbulent when Reynolds Number becomes greater than three $\times 10^6$ [7].

2.6   BOUNDARY LAYER

A thin layer of viscous fluid developed when it flows over the solid surface. The velocity of fluid varies from zero at the surface to free stream value away from the surface. This boundary layer has some thickness δ from the surface, defined as the distance perpendicular to the surface at which velocity value achieve free stream value.

The boundary layer is of two types.

- **Laminar boundary layer.**
- **Turbulent boundary layer.**

The laminar boundary layer is also known as the layered boundary layer, which develops at low Reynolds.

$$Re = \frac{intertial\ forces}{viscous\ forces}$$

For low Reynolds number, viscous effects are dominant over the inertial forces. Hence it is more layered, i.e., each layer slides over an adjacent layer. Any exchange of mass and momentum only occurs between adjacent layers, visible only on the microscopic scale.

While for the turbulent boundary layer, fluid particles have more inertial forces than viscous forces and its boundary layer is more prominent than the laminar boundary layer. In a turbulent regime, layers of fluid diffuse into each other. Hence their mass and moment transfer is visible.

In the laminar regime, velocity change is uniform as it moves downstream from the leading edge. However, in a turbulent regime, velocity change is unsteady and has swirling flows inside the boundary layer.
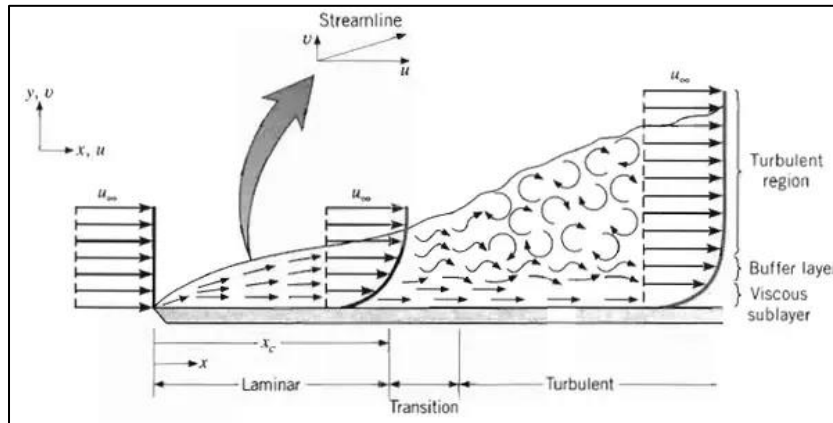

Figure 2.3 Boundary layer formation due to no-slip condition [8].

In the figure, the velocity profile in turbulent flow is much fuller than laminar flow, with a sharp drop near the surface. The turbulent boundary layer can be considered to consist of four regions characterized by the distance from the wall. The very thin layer next to the wall where viscous effects are dominant is the viscous sublayer. The velocity profile in this layer is very nearly linear, and the flow is streamlined. Next to the viscous sublayer is the buffer layer, in which turbulent effects are becoming significant, but viscous effects still dominate the flow. Above the buffer layer is the overlap layer, in which the turbulent effects are much more significant but still not dominant. Above that is the turbulent layer in which turbulent effects dominate over viscous effects.

2.6.1 FLOW SEPARATION

Due to boundary layer formation, a frictional force resisting the fluid flow over the surface. This cause to drastically decreases in velocity nearer the surface to zero and a uniformly increase in the y-direction to the surface, as shown in figure 2 above. When the fluid particles do not have any energy (viscous forces are dominant on inertial forces), the flow starts to separate. Take an example

of an airfoil. When fluid interacts with the airfoil at the leading edge (stagnation point), the fluid velocity is zero. However, downstream of the pressure decreases drastically, and at a certain point, velocity is maximum. Downstream of that point to trailing edge pressure starts to increase, for completely attached flow, the rearward pressure and frontal pressure are equal, resulting in no pressure drag called form drag.

Nevertheless, pressure starts to increase downstream to the trailing edge in the actual case, resulting in an inverse pressure gradient. Fluid particles have to work their way uphill against the increasing pressure. Due to boundary layer formation, a frictional force resisting the fluid flow over the surface. This cause to drastically decreases in velocity nearer the surface to zero and a uniformly increase in the y-direction to the surface, as shown in figure 2 above. When the fluid particles do not have any energy (viscous forces are dominant on inertial forces), the flow starts to separate. Take an example of an airfoil. When fluid interacts with the airfoil at the leading edge (stagnation point), the fluid velocity is zero. However, downstream of the pressure decreases drastically, and at a certain point, velocity is maximum. Downstream of that point to trailing edge pressure starts to increase, for completely attached flow, the rearward pressure and frontal pressure are equal, resulting in no pressure drag called form drag. Nevertheless, pressure starts to increase downstream to the trailing edge in the actual case, resulting in an inverse pressure gradient. Fluid particles have to work their way uphill against the increasing pressure.

Hence fluid particles slow down for particles outside the boundary layer. But in the boundary layer, fluid particles already have a small velocity due to friction forces. This uphill cause them to reverse their direction because they do not have the energy to contract this increasing pressure. This reversal in a direction generally causes flow separation.

The consequences of flow separation:

1. **Drastic increases in drag, caused by form drag due to flow separation.
2. **A drastic loss in the lift.
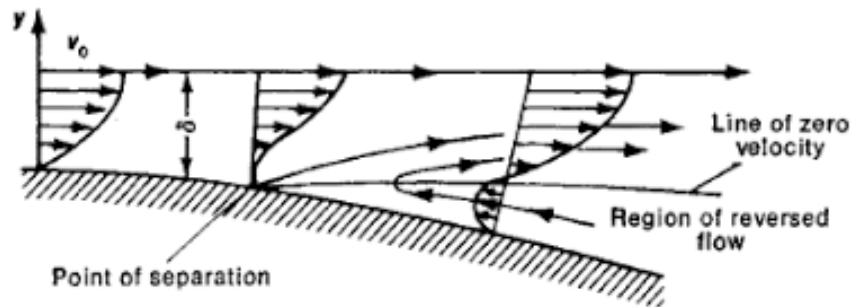
Figure 2.4 Flow Separation [9].

2.7 Laminar Separation Bubble

The airfoil operating in the low Reynolds' number flow, called Laminar Separation Bubble, may be affected by the intermediate layer splitting and reinstallation. A negative pressure gradient causes the separation and transition between the boundary layer and the turbulent flow of the laminar. In the high Reynolds flow, the airflow remains thoroughly turbulent throughout the airfoil. However, the turbulent flow can touch and attach the surface in the low Reynolds flow, forming the Laminar Separation Bubble. The volume of the divided laminar and turbulent flux nearly does not interchange energy with the external flux, minimizing the lifting and drag of the airwaves [10].

3 Numerical Methods

The CFD procedure focuses on numerical approaches. Researchers focus on CFD, physical modelling and numeric, two key elements. We seek a range of equations or mathematical relationships in physical modelling to close the governing equations. One is interested in designing new equations for the additional unknowns resulting from the averaging process for turbulence modelling, for example.

In numerical methods, the focus is on developing efficient, robust, and reliable PDE solution techniques. PDEs are a mixture of differential terms (change rates) that describe a principle of conservation. PDEs can describe all physical processes without loss in general. In the CFD process, the regulating PDEs, i.e., derived algebraic equivalents that would properly depict the original PDEs, are discrete. This is achieved by converting each differential term into an algebraic equation. There exist serval methods to convert differential equations into PDEs, such as:

- Finite Differencing Method
- Finite Element Method
- Finite Volume Method
- Spectral Method

The CFD Finite Volume Method FVM is preferable because it fulfils conservation laws by nature. The FVM divides a region of arbitrary flow into many smaller volumes, called cells that form the entire Mesh. Each cell has a solution approximate for each equation resolved on the computer grid at a particular time. The FVM takes information from the neighboring cells according to the discretization method used. Boundary conditions are used on the cells that face the flow domain. Moreover, initial conditions are used to compute solutions for the first-time step [11].

3.1 Navier-Stokes equations

The main equations guiding the fluid flow are the Navier-Stokes equations. Those equations that are a series of couplings of non-linear partial differential equations quantitatively explain fluid flow problems. They are a series of non-linear partial differential equations that define the viscous fluid movement by expressing mass, momentum, and energy preservation in any control volume (Patankar, 1980). However, this research does not include thermal processes to avoid applying the energy equation.

The continuity equation (conservation of mass):

$$\frac{\partial u_i}{\partial x_i} = 0$$

the momentum equation (conservation of momentum):

$$\frac{\partial u_i}{\partial t} + u_j \frac{\partial u_i}{\partial x_j} = -\frac{1}{\rho}\frac{\partial p}{\partial x_i} + \frac{\partial}{\partial x_j}\left(v\frac{\partial u_i}{\partial x_j}\right)$$

$\frac{\partial(u_i)}{\partial t}$ acceleration term

$\frac{\partial(u_j)}{\partial x_j}$ convection term

$\frac{\partial p}{\partial x_j}$ pressure gradient

$\frac{\partial}{\partial x_j}\left(v\frac{\partial U_i}{\partial x_j}\right)$ Effects of viscosity

where t is the time, ρ is the flow density, p is the pressure, v is the kinematic viscosity.

3.2 Turbulence models

Every flow gets turbulent above a particular number of Reynolds. This means that the impact of turbulence is achieved when the Reynolds number of laminar flows is increased sufficiently. The majority of engineering flows are in the wild. Turbulence must therefore be considered. Turbulence is usually created by certain kind of disturbance, like flow around an object, fluctuation, and randomly fluency in speed fields over a wide variety of lengths and time scales. The varying speeds generate an eddy. However, the local average speeds and other fluid parameters can be detected despite the altered, chaotic oscillations. The controlled fluid flow

equations, along with boundary and start conditions, describe any flow situation fully. However, even for the most straightforward turbulent flow, no analytical answer exists. By solving the Navier-Stokes equations with numerical methods, the local flow properties of complicated flows are determined.

There are mainly three approaches to predict turbulence behaviors are the Direct Numerical Simulation (DNS), Large Eddy Simulations (LES) and Reynolds averaged Navier-Stokes (RANS).

3.2.1 Direct Numerical Simulation (DNS)

A DNS tries to resolve all flow regimes incomplete by resolving Navier-Stokes's equations up to the scales of Kolmogorov. However, the demand for computing resources becomes relatively high due to mesh resolution and time step size. Therefore, due to a shortage of computer capacity, only a few simple cases were solved with DNS. Moin and Mahesh provide a helpful review of the work and contributions of DNS [12].

3.2.2 Large Eddy Simulation (LES)

In 1963, Joseph Smagorinsky presented an alternative way to simulate the high number of turbulent flows. The broad motions (large eddies) of the turbulent flow are resolved in LES, while small scales are simulated with sub-grid scales. LES is less than DNS but is greater than RANS computer costs. The LES is formed through the filtering process resulting in the damping of high-frequency, temporal or spatial oscillations using the integration of Navier-Stokes equations with a filter function. (Worthy, 2003) (Zhiyin, 2015) [13].

3.2.3 Reynolds Average Navier-Stokes (RANS)

Reynolds Averaged Navier Stocks (RANS) equations are the most computer-based way to fix turbulence. The RANS approach models all the turbulence scales, including grid resolution and not a turbulent scale, in the order of the mean flow. Compared to DNS and LES, this gives enormous computer savings. All the instability is averaged, all seen as a permanent phenomenon in Reynolds' averaged approach to turbulence.

The Navier-Stokes equation can be time-averaged over a period T large enough to mean the turbulent fluctuations to obtain the Reynolds Averaged Navier-Stokes (RANS) equations. To form the Reynolds-Averaged equations, the variables U and p are written as the sum of a mean $\overline{U}, \overline{p}$ and its fluctuating part u', p'.

$$U = \bar{U} + u'$$

$$p = \bar{p} + p'$$

Substituting the above equations into Navier-Stokes equations then we could produce RANS equations form:

Continuity equation

$$\frac{\partial \bar{U}_i}{\partial x_i} = 0$$

Inserting the Boussinesq hypothesis into the momentum equation yields

$$\frac{\partial \bar{U}_i}{\partial t} + \bar{U}_j \frac{\partial \bar{U}_i}{\partial x_j} = -\frac{1}{\rho}\frac{\partial \bar{p}}{\partial x_i} + \frac{\partial}{\partial x_j}\left[(v + v_t)\frac{\partial \bar{U}_i}{\partial x_j}\right] - \frac{\partial}{\partial x_j}(\overline{u_i u_j})$$

Turbulent viscosity assumption

$$-\overline{u_\iota u_J} + \frac{2}{3}k\delta_{ij} = v_t\left(\frac{\partial \bar{U}_i}{\partial x_j} + \frac{\partial \bar{U}_j}{\partial x_i}\right)$$

RANS equations transform Navier Stokes equations into six unknown terms, so-called Reynolds stresses. To solve the case, new extra models need to be included to model such six new terms.

RANS models are categorized depending on the extra variables that are added:

1. **Zero equation model:** Model for mixing length in this model, the turbulent viscosity, the local fluid speed, and the distance to the nearest wall are regarded as computing only two parameters. This is the least but also the least accurate computationally intense method, yet it provides good approximations for internal flow.

2. **One equation model:** This low-Reynolds numbers of models add a single additional variable for the viscosity of Spalart-Allmaras, created for aeronautical uses, and do not have any wall functions. It is highly stable and convergent but without precise cuts when there are shear flow, separate flow, or decaying turbulence.

3. **Two equation models:** For two additional variables, k-epsilon models solve the turbulent kinetic energies and the kinetic energy dissipation rate, whereas wall functions are

available. These models are the most common in the industry since they show good convergence and inexpensive computing costs. These models work well with external flows via complex geometries, but they lack precision in flux fields with unfavorable pressure gradients.

In this section, we discuss the standard k-epsilon.

3.2.4 Spalart Allmaras Turbulence model

Spalart Allmaras is a RANS turbulence model with one equation. Since the previous k epsilon model, it is created for aerodynamic flows, and the boundary layer was not resolved sufficiently. For the calculation of Reynolds, the model uses the Boussinesq equation [14]. A linear eddy viscosity model is the general SA model with eddy viscosity linked to $\tilde{v}$.

$$\mu_t = \rho f_{v1} \tilde{v}$$

$$\frac{\partial(\rho\tilde{v})}{\partial t} + div(\rho\tilde{v}\boldsymbol{U})$$

$$= \frac{1}{\sigma_v} div\left[(\mu + \rho\tilde{v})grad(\tilde{v}) + C_{b2}\rho\frac{\partial\tilde{v}}{\partial x_k}\frac{\partial\tilde{v}}{\partial x_k}\right] + C_{b1}\rho\tilde{v}(\Omega + \frac{\tilde{v}}{(\kappa y)^2}f_{v2})$$

$$- C_{w1}\rho\left(\frac{\tilde{v}}{\kappa y}\right)^2 f_w$$

Whereas,

$$\Omega = \sqrt{2\Omega_{ij}\Omega_{ij}} = mean\ vorticity$$

And

$$\Omega_{ij} = \frac{1}{2}\left(\frac{\partial U_i}{\partial x_j} - \frac{\partial U_j}{\partial x_i}\right) = mean\ vorticity\ tensor$$

The function

$$f_{(v1)} = f_{v1}\left(\frac{\tilde{v}}{v}\right)$$

$$f_{(v2)} = f_{v2}\left(\frac{\tilde{v}}{v}\right)$$

$$f_{(w)} = f_w \left(\frac{\tilde{v}}{\widetilde{\Omega} \kappa^2 y^2} \right)$$

Are wall damping function and the model constants are,

σ_v	κ	C_{b1}	C_{b2}	C_{w1}
1.5	0.4187	0.1355	0.622	$C_{b1} + \kappa^2 \dfrac{1 + C_{b2}}{\sigma_v}$

These model constants have been tweaked for external aerodynamics fluxes. The employment of a turbulence model such as Spalart Allmaras in a low Reynolds number over an airfoil or propeller requires a high degree of refining near the airfoil's wall [14]. In the presence of unfavorable pressure gradients, model and model constants were demonstrated to be successful. The model and model constants proved to be successful in the presence of adverse pressure gradients.

3.3   Computer Modelling Software

Computer-based simulations analyze computational fluid dynamics for systems including fluid flow, heat transport, chemical processes, etc. OpenFOAM has several advantages for free, open-source simulations of Computational Fluid Dynamics (CFD) and can run on massive processor arrays in parallel. Every user has the authority to modify existing code or create their code suitable to their needs and share results and conclusions with other users, without the restriction of licenses or any other limitation by being an open source that allows users to personalize their functions software. CFD packages typically have three essential components: a pre-processor, an after processor and a solver. The Mesh is built, and the boundary conditions and fluid properties are set up in the pre-processing step. The solver then does the flow analysis and shows the estimated findings with various data visualization tools in the post-processing section. The purpose of this thesis is to illustrate and test the use of the steady-state Reynolds Averaged Navier-Stokes (RANS) solver in OpenFOAM (simple form application) by applying it to three different roof incident ger structure cases.

The first part of the report provides a detailed description of the basic file structure used for all OpenFOAM simulations. The content and purpose of each of the files are discussed, as are some of the valuable utilities. Next, an overview of the OpenFOAM RANS solver, in a simpleFoam, is

provided. This includes a description of how the equations are discretized and the algorithms used to solve the resulting matrix equations.

Appropriate boundary conditions are described for both models, and the simulated results are compared with international standards results. The improvement can be obtained using more refined meshes, and the design change is demonstrated.

3.3.1   OpenFOAM and its applications

Open-Source Field Operation and Manipulation, abbreviated as OpenFOAM, is a computational open-source dynamics collection of C++ libraries and algorithms intended to do numerical modelling of sound and fluid mechanical issues. OpenFOAM is dispersed across a broad spectrum of issues with various solvers and tools. However, because of the open-source nature of OpenFOAM, users can create their algorithms and solutions for their situations or change current solvers. In addition, OpenFOAM is set up in a specific folder structure utilizing texting files. For the OpenFOAM case file, the basic structure is as follows,
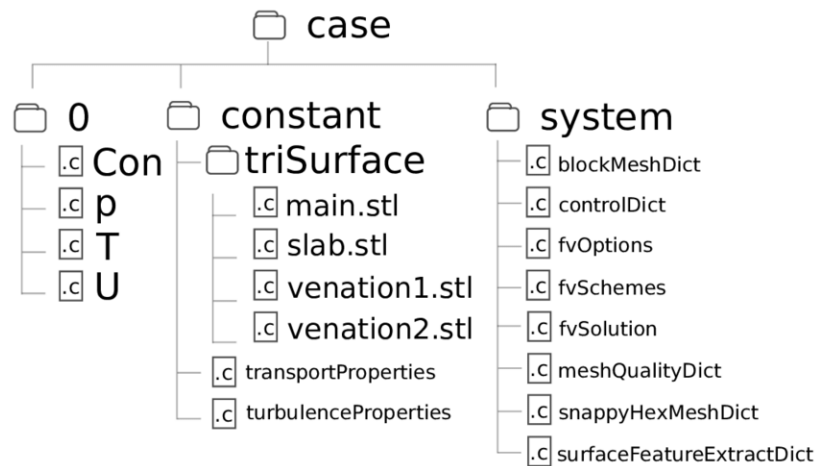

Figure 3.1File structure of typical OpenFOAM simulation [15].

In general, an OpenFOAM case consists of three directions named system, constant and 0.

3.3.2 System folder

The system directory contains three files which are the control diet, fvSchemes and fvSolution files.

In the controlDict file, the overall running of the simulations is set, including start/end time and time step. For a steady-state solver, the start time and end time identify the start and end of the iteration loop, and the time step is the iteration counter.

In fvSchemes file, the numerical schemes for terms are set. The discretization schemes used for the time dependence, divergence, Laplacian, and gradient terms are all solved numerically.

In the fvSolution file, the numerical solvers for each equation are specified by the user. For a general, three classes of iterative solvers are available in OpenFOAM:

- PCG – Preconditioned conjugate gradient method
- GAMG - Geometric algebraic multigrid method
- smoothSolver – the Gauss-Seidel method.

The matrix solvers are iterative and based on a number of iterations reducing the residual equation to a default value. The residual is assessed by replacing the present solution with the equation, taking the different size between the left and right sides, and being standardized to make it irrespective of the scale of the investigated problem. The initial residual is assessed based on the present values of the field before resolving an equation for a given field. The user can define an absolute tolerance as well as a relative tolerance. The residual is reassessed after every solver iteration.

1. The residual falls below the absolute tolerance.
2. The ratio of current to initial residuals falls below a specified relative tolerance, relTol.

The absolute tolerance represents the level at which the residual is small enough that the solution is sufficiently accurate. The solver relative tolerance limits the relative improvement from the initial to the final solution.

3.3.3 Constant folder

Two files (transport properties, turbulence properties) and a folder (poly mesh) are placed in this folder.

The file transport properties describe the properties of the fluid. For a steady-state incompressible solver, only the kinematic viscosity ν is required. Note that OpenFOAM's incompressible solver works at kinematic pressure p/ρ where ρ is the air density.

In the file turbulenceProperties, the turbulence model and its parameters are set.

In polyMesh sub-directory contains all the files describing the geometry and the Mesh. The mesh generation can be created in various ways. This includes OpenFOAM provided utilities which are blockMesh and snappyHexMesh and allowing third party meshes to be imported.

3.3.4   0 folder

This folder has boundary conditions. However, in addition to typical boundary conditions, such as velocity and pressure, we should include many different boundary condition files depending on the turbulence model we use. The relevant p, U, k, and epsilon files for a constantly running RANS simulation using k-β turbulence models. In addition to supplying a patch name in the boundary file for the corresponding patches. Therefore, a nutWallFunction type should be specified in the Nut File on the wall boundaries, an epsilonWallFunction on the equivalent patches in the epsilon file, and a kqRwallFunction on the appropriate patches in the k file.

3.3.5   PIMPLE and SIMPLE Algorithm

PimpleFoam and simpleFoam are a solution for an unstable, turbulent flow used to calculate the flow with the PIMPLE algorithm. When the RANS Turbulence technique causes unstable problems, turbulent problems are regarded as highly unstable. Based on our problem, as we do not know if the flux within the cavity is steady, we treat it as a temporary problem in computational fluid dynamics. This combines these underlying differential equations and makes it impossible to resolve them directly. By using the discretized equations. The only choice is the iterative technique.

For that purpose, PIMPLE and SIMPLE algorithm is best suited for the characteristics of the problem.

1. Set the boundary conditions specified in the 0 directories.
2. Gradients of velocities and pressure are computed.
3. The discretized momentum equation is solved so that it can compute the intermediate velocity field.

4. Compute the uncorrected mass fluxes at the cells faces.

5. The pressure correction equation is solved to produce cell values of the pressure correction (p^*).

6. The pressure field is updated based on the following method,

$$\mathcal{M}U = -\nabla P$$

Where $\mathcal{M}$ is the coefficient matrix, from which the diagonal matrix will be extracted and named as $\mathcal{A}$. An inverse of $\mathcal{A}$ is taken and named as a_p. After the extraction, we manipulate the above equation and get,

$$\mathcal{M}U = \mathcal{A}U - \mathcal{H}$$

And

$$\mathcal{H} = \mathcal{A}U - \mathcal{M}U$$

By doing some mathematics, we get the following equation which will be used to calculate the corrected pressure,

$$\nabla.(\mathcal{A}^{-1}\nabla P) = \nabla.(\mathcal{A}^{-1}\mathcal{H})$$

7. Based on the corrected pressure, the fluxes at the cell faces are calculated.

$$U = \mathcal{A}^{-1}\mathcal{H} - \mathcal{A}^{-1}\nabla P$$

8. The above loop is repeated until the residuals of the above equations fall below the mentioned tolerances.

3.4 Grid Generation

Grid generation is an essential component of most CFD pre-processors Packages. - Packages. The number dramatically affects the exactness of a CFD solution of the grid cells. A finer grid tends to be a better solution by calculation costs are growing in areas with optimal meshes for variances and coarser for minimal changes in areas of minimal change, wide variances and coarser. It is up to the moment. CFD user designs a grid appropriate for the particular scenario.

The boundary layer can be determined relatively quickly in an external flow, but it can be more challenging to discern the enhanced cell refinement around the model surface. Y+ is the non-dimensional distance between the surface of the model and the first cell node. It takes care of the wall's fluid movements, characteristics, geometry, and friction, so that the greatest level of

refinement level in one Mesh may be established. To build the perfect Mesh, a minimal computer mesh with high accuracy simulations can be achieved utilizing the first layer calculated using an acceptable y+ value and smooth transition to the background mesh.

3.4.1   Boundary-Layer calculation

Calculation of y+ can be done with the skin friction coefficient at the wall. The skin friction coefficient is dependent on Reynolds Number as follow,

$$C_f = \frac{0.026}{Re_x^{\frac{1}{7}}}$$

Using the friction coefficient, wall shear stress is calculated at the wall as follow,

$$\tau_{wall} = \frac{C_f \rho U_\infty^2}{2}$$

Then the frictional velocity at the wall is calculated, which helps to estimate the first layer height,

$$U_{fric} = \sqrt{\frac{\tau_{wall}}{\rho}}$$

$$\Delta s = \frac{y^+ \mu}{U_{fric} \rho}$$

The development of unfavorable pressure gradients needs the initial height of the cell within the viscous sublayer in aerodynamics and airfoils that operate in a transitional or turbulent flow. A y+ value of less than 1 with the Spalart Allmaras turbulence model is y+.

4 Staaker BG-200

4.1 System description

The BG-200 is a coaxial octocopter, as depicted in Figure 4.1. The default settings for the propeller are 28"X9.2" both as top and bottom propellers with a 109.2 mm axial spacing.

The BG-200 has a maximum weight of 25 kg, according to Unmanned Nordic. The minimum volume is 16 kilograms (8.5 kg drone and 7.5 kg battery). A theoretical maximum volume of 60 min without payload [16], see BG-200 Technical Block, which uses 31 Ah standard batteries. This thesis focuses on the propeller configuration, among other strategies to boost Staaker endurance.

4.2 Propeller Configuration

The Staaker is a coaxial octocopter, shown in figure 4.1, with four G28 x 9.2 coaxial rotor configurations. The propeller's diameter and pitch are 711.2 mm and 233.7 mm, respectively, as shown in Table 4.1. Pitch is described as a rotational distance unit. In this scenario, in one horizontal spin, the propeller moves 233,7 mm up.

Figure 4.1 Staaker BG-200 [17].

Table 4.1 Propeller characteristics.

Propeller Name	Diameter	Pitch
28U 28L	$711.2 mm$	234 mm

4.3   Reverse Engineering

In order to simulate this propeller, reverse engineering is used. Reverse engineering provides a mechanism for automated collection from a physical object of three-dimensional data. Digital documentation and 3D modelling can be divided into two parts.

A handheld triangulation scanner was used by Free form's Handy scan 3D (700) to document the propeller digitally. Through 3D scanners, the data point coordination on an object surface is estimated either by a line or a point. It is not necessary to confuse the triangulation scanner with a triangle mesh. 3D scanner triangulation refers to the item point, the position of the laser diode and the camera position. The digital documentation process creates a point cloud with millions of data points. VX components generate a triangular mesh by collecting coordinates of the data points using the Handy scan 3D linked program. The Handy scan 3D creates a triangular mesh with a precision of 0.025 mm. According to Freeform, in digital documentation, a dot cloud with millions of data points is created. By collecting the data points coordinates using the Handy scan 3D connected software, VX components build a triangular mesh. With a precision of 0.025 mm according to Freeform, the Handy scan 3D creates a triangle mesh. The data triangulation mesh is installed in the digital documentation phase and gives a vast range of essential data points for digital tracking and re-construction.

 Propellers were separated into ten sections by the Autodesk Inventor from hub to wingtip. In order to generate an airfoil using an interpolation curve, points along the cross-section were selected. The digital documentation phase has had some difficulty characterizing both the leading and following edges precisely. An interpolation curve allows a more precise understanding of the curve on both borders. The loft function has been utilized to interconnect all cross-sections. As rails for the loft function, two guidelines were laid on the leading and trailing edges. Since just one side of the propeller is created from a hub to a wingtip, the half propeller has been replicated and rotated 180 degrees along the z-axis, provided the propeller is located in the xy plane with origin in the middle of the hub. The digital propellers have been exported to an OpenFOAM file type. ASCII STL file type has been utilized for convenience. In the clockwise and counterclockwise versions of Table 4.2, CW and CCW refer to the rotary direction of the propeller. Because the coaxial configuration is counter-rotating, each propeller is reflected and called CCW. There is also an average angle of attack. The mean values from the end of the hub to the wingtip are obtained.

Table 4.2 3D propeller models.

Propeller Name	File type	Diameter	Pitch	AOA
28U 28L CW	.stl	$711.2mm$	234 mm	11.9^0
28U 28L CCW	.stl	$711.2mm$	234 mm	11.9^0

4.4 Axial Separation

The conventional coaxial rotor arrangement has an axial spacing of 109.2mm. The minimum axial separation is 50mm with integrated rotors and 230 mm with the farthest distance.

4.5 Flight conditions

Their flight endurance Staaker BG –200 is estimated to be 60 min with a weight of 16 kg by Nordic Unmanned [15]. This weight must be counteracted by the combined thrust of all the propellers to stand still in the air. In the US, laboratory experimental data gave data such as gram force (GF) for vertical thrust, rotating speed as rounds per minute, Newton meter torque and other battery and power-using statistics. Table 4.3 shows the four propellers and typical coaxial propeller setup using the RPM, and the time at a vertical thrust corresponds to 4000 grams of strength (39.2 N). Table 4.3 displays experimental data from the UiS machine laboratory. The vertical thrust must be one-fourth of the combined vertical thrust in each coaxial propeller setup to hover (16 kg). In contrast, the single rotor propeller in table 4.3 has been adjusted to indicate the highest contribution of coaxial setups in the hover.

Table 4.3 Rotor Configuration.

Configuration	Propeller	Thrust [N]	Torque [Nm]	RPM	Contrib.
Coaxial Setup	Upper	23.82	0.85	2000	0.63
28U 28L	Lower	15.53	0.73	2000	0.27

4.6 Reynolds Number

The Reynolds Number can be used to determine the flow condition of the diverted free stream across the propeller blade to determine the flight condition of the octocopter. The Reynolds number can be determined from the surface area of the equations, density, kinematic viscosity, and velocity. The speed may be computed with RPMs in Table 4.3, and the chord line of the 3D propeller model specified in Table 4.1 can be measured and calculated Re values. And kinematic

viscosity under standard atmospheric circumstances. RPM speed can be determined in Table 4.3, and the 3D propeller chord line can be measured as indicated in Table 4.1.

A turbulence model is necessary to solve turbulence as the propeller is in a laminar, transitional, and turbulent flow. In a 2D test case, the correct turbulence model and grid refining levels will be selected along the borders in the next chapter. The challenge can be how to select an appropriate CFD system to test all previously discussed options in this chapter. The Research Center NASA Langley has turbulence modelling resource to limit the number of steps that can offer CFD developing sources accurate and up-to-date RANS model information and ensure that models are appropriately implemented. This thesis will justify the selection of turbulence models in combination with a practice of Grid Convergence.

5 Simulation of the 2D airfoil

The validation of results is a vital component of any simulations. For that purpose, we will perform case validation for our studies using the 2D airfoil. NACA 4412 airfoil is one of the most popular airfoils use for validation. The experimental data of NACA 4412 is compared with the OpenFOAM results obtained from the implantation of turbulence model Spalart Allmaras with different gird sizes.

5.1 Validation of a 2D case

In this practice, the validation of our case will be performed. The CFD simulation of NACA 4412 airfoil will be performed at the operating condition of Reynolds Number $1.52\ million$ with the speed of $27.13m$ having the chord of $0.912m$ and kinematic viscosity of $1.605e - 5m^2/s$. The experimental data for different turbulence models are available at the NASA Turbulence Modelling Resource [17]. We just took the data for Spalart Allmaras, with the .dat file available on their site. Projected results with the same turbulence model are,

1- For CFL3D: $c_l = 1.7210, c_d = 0.0286$
2- For FUN3D: $c_l = 1.7170, c_d = 0.0294$

Whereas $c_l\ and\ c_d$ is the lift and the drag coefficient of an airfoil. These are values for the turbulence model Spalart Allmaras. For our case, we chose the same initial and boundary conditions. In the CFD analysis performed by NASA, the far-field was chosen to be a hundred times the chord length of the airfoil.

5.2 Case setup

5.2.1 Model Configuration

The NACA 4412 airfoil coordinates were imported from the website Airfoil Tools, and with the help of an Excel Sheet, shown in figure 5.1. Airfoil geometry was created in CATIA V5 and converted into a .stl file. Then the .stl file was imported into the .stl file editor and the airfoil tilted with 13.87^0 the angle of attack.
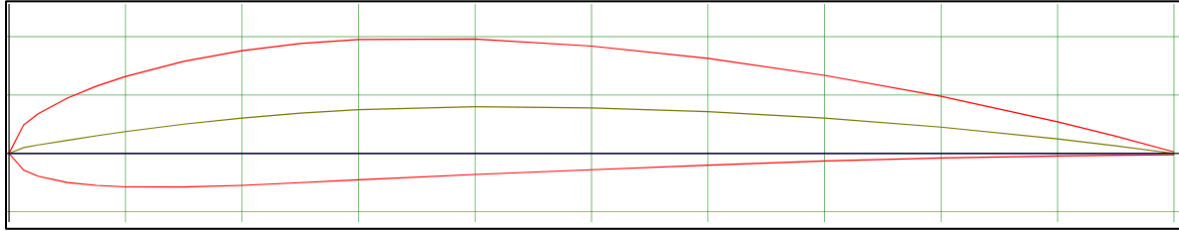
Figure 5.1 Geometry of NACA 4412 airfoil [20].

5.2.2 Grid Generation

Meshing is the most crucial step in CFD, the quality of Mesh has a significant influence. Corser mesh than the optimal limit can give spurious results; however, fine Mesh can lead to computational cost on the other side. Hence, while generating a grid, many parameters are kept in mind. For the case of airfoil or wing CFD, the spacing of the near-wall cells is essential. As we know, near the wall, due to friction, no-slip condition holds, which cause the adverse pressure gradient. To get the best accurate results, we always want to be in the viscous sub-layer of the boundary layer. For that purpose, the value of y+ should always be less than one.

Furthermore, the number of layers should be taken under consideration because it also affects the capturing of boundary layer separation. For that purpose, we took the $y+< 1$ with a reasonable number of layers. For that purpose, the value of y+ should always be less than one. Furthermore, the number of layers should be taken under consideration because it also affects the capturing of boundary layer separation. For that purpose, we took the $y+< 1$ with a reasonable number of layers.

The domain for meshing was chosen to be $25m \times 25m$ in $x \times y$ direction. Moreover, the airfoil part is subtracted from the domain. The blockMeshDict was utilized to create the initial domain with enough cells, and later the snappyHexMesh tool was utilized to create the actual Mesh. The grading method was used to save the computational cost, the Mesh is refined in most abrupt changes, and the coarse Mesh is used where there are no sharp variations in fields. For that purpose, three refinement regions were defined, at points $(0.9, 0.03)$ and $(1.1, 0.08)$ with refinement level of 4 giving the cell size of $1.01e - 3m$, $(-0.15, -0.2)$ and $(1.3, 0.2)$ with the refinement level of 3 giving the cell size to be $4.06e - 3m$, $(-0.5, -0.7) and$ $(2, 0.6)$ with the refinement level of 2 generating cell size to be $0.016m$. The name of boundaries and patches are defined in

blockMeshDict, and the domain is discretized in cells. Based on the size of cells, the refinement is performed in snappyHexMeshDict. Once the blockMesh is created, the next task is to find the spacing of near-wall cells. For that purpose, the calculation is performed for Reynolds Number, and the relation of near-wall cell spacing with $y+$ is calculated. The calculations are performed below.

First, the value wall friction coefficient is calculated.

$$C_f = \frac{0.026}{Re_x^{\frac{1}{7}}}$$

For $Re = 1.52\ million$, we get.

$$C_f = 3.378e - 3$$

After that wall shear stress is calculated,

$$\tau_{wall} = \frac{C_f \rho U_\infty^2}{2}$$

$$\tau_{wall} = 1.447$$

Calculating friction velocity,

$$U_{fric} = \sqrt{\left(\frac{\tau_{wall}}{\rho}\right)}$$

$$U_{fric} = 1.15\ m/s$$

Then using the relation of wall spacing,

$$\Delta s = \frac{y^+ \mu}{U_{fric} \rho}$$

We get the relation,

$$\Delta s = (1.437e - 5) \times y^+$$

Now, based on the value of y^+ the near wall spacing is calculated. First, a basic mesh will be used with a certain y^+ value, and then for grid convergence, we will change the value of y^+ Moreover,

the refinement level of the grid to get the optimal Mesh. Table 5.1 shows the parameters chosen for the first grid.

Table 5.1 Initial Mesh Parameters.

Domain size	$25\ m \times 25\ m$
Refinement Level 0 Thickness	$0.26\ m$
Value of y^+	0.4670
First layer Thickness	$6.710e - 6\ m$
Expansion Ratio	1.3
Number of Layers	16
Final Layer Thickness	$2.06e - 5\ m$
Highest Refinement Level on the Wing	9
Highest Refinement level thickness	$9.92e - 7\ m$
Number of Cells	53484

As mentioned earlier, there is a total of 3 refinement regions. However, on the wing, we have increased the refinement level to capture the complex flow. Furthermore, the number of surface layers helps to capture the adverse pressure gradient due to friction of the wall. The domain and the geometry are shown in figure 5.2, 5.3 and 5.4,
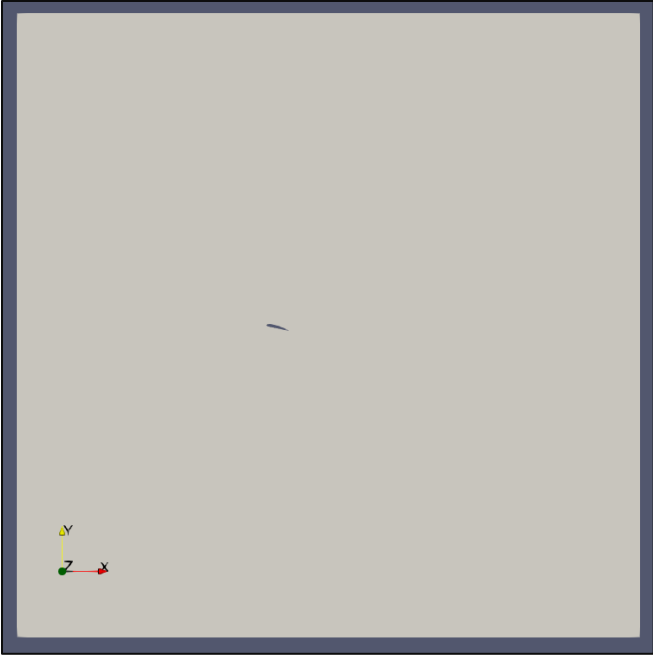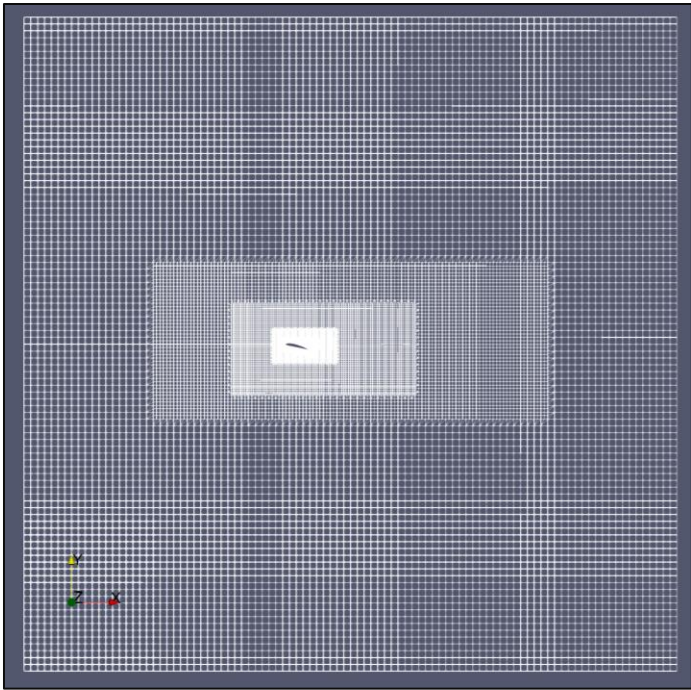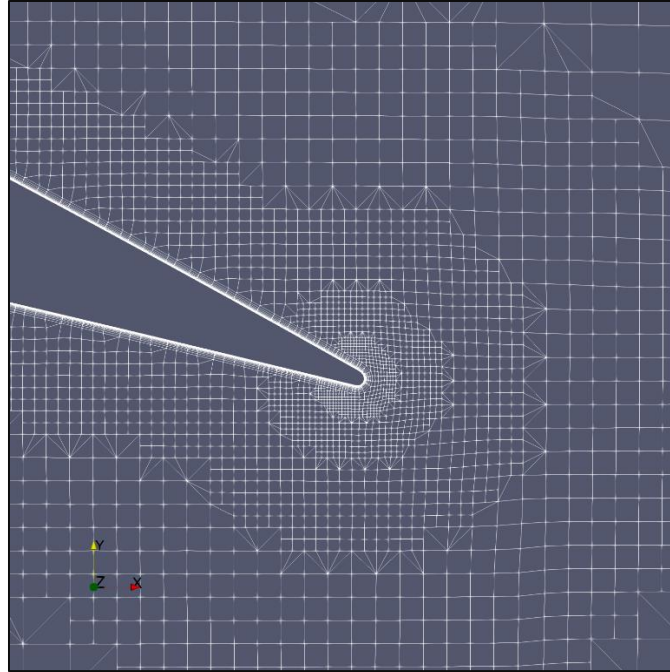
Figure 5.2 Fluid domain.

Figure 5.3 Grid.

Figure 5.4 Surface Layer near the wing.

5.2.3 Case Setup

A steady-state solver simpleFoam was selected for the simulation of flow over the airfoil, for the inlet velocity the $27.13\ m/s$ and for the outlet, the pressure of $0\ guage\ pascal$ was initialized. The top and bottom patches were defined as far-filed, so to nullify any effect, a slip condition is given. For front and back, the empty condition was used so that the case remains two dimensional. The Spalart Allmaras model was used, with a Reynolds Number of $1.52\ million$.

5.2.4 Discretization and Solver Setting

FvSchemes and fvSoultion files show the discretization schemes and the solvers utilized for each matrix equation in the standard Spalart Allmaras simulation for OpenFOAM. The controlDict will carry out 3,000 iterations, and each 100th iteration will be written. The following schemes are described in table 5.2.

Table 5.2 Discretization Schemes.

Time Schemes	*steadyState*
Gradient Schemes	*Gauss linear*
Divergence Schemes	*Gauss limited linearV* 1
Laplacian Schemes	*Gauss linear limited* 0.5
Surface Normal Schemes	*linear*

A SIMPLE algorithm was implemented, which is suitable for steady, incompressible, and turbulent flows. The tolerances were set in the fvSolution dictionary, at 1×10^{-6} with relative tolerances of 0.1 to ensure the solver does not stop until the convergence criteria are achieved.
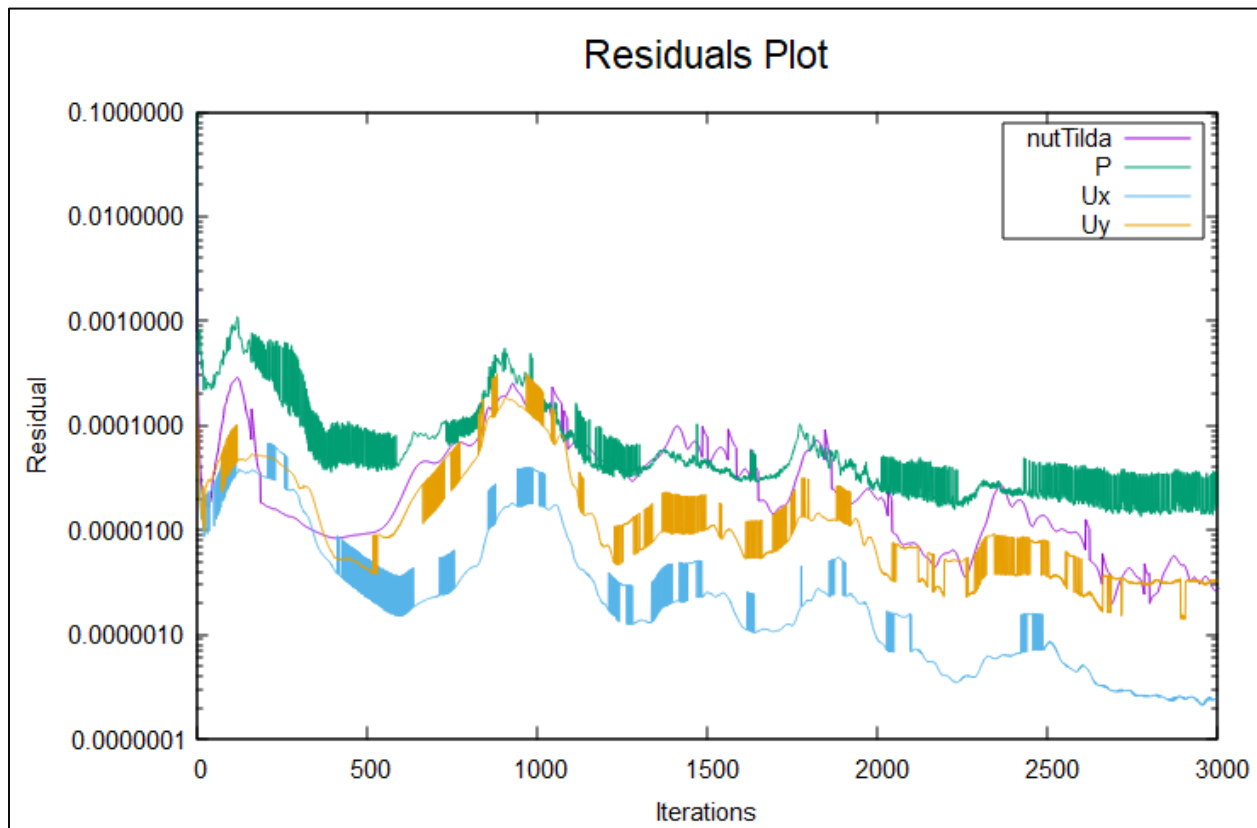
5.2.5 Residual Plot

Figure 5.5 Residuals Plot vs Iterations.

The residual is shown in figure 5.5, that the error for velocity and pressure has been reduced below tolerance level. However, pressure has a bit high residual level than the rest of the parameters because it the most sensitive parameter.

5.2.6 Results

We found that the simulation results show good agreement with the experimental results obtained from the NASA Turbulence Modelling Resource [18], as shown in figure 5.6. Hence, from the results, it can be concluded that solver settings with the initial grid prove reasonably accurate results.
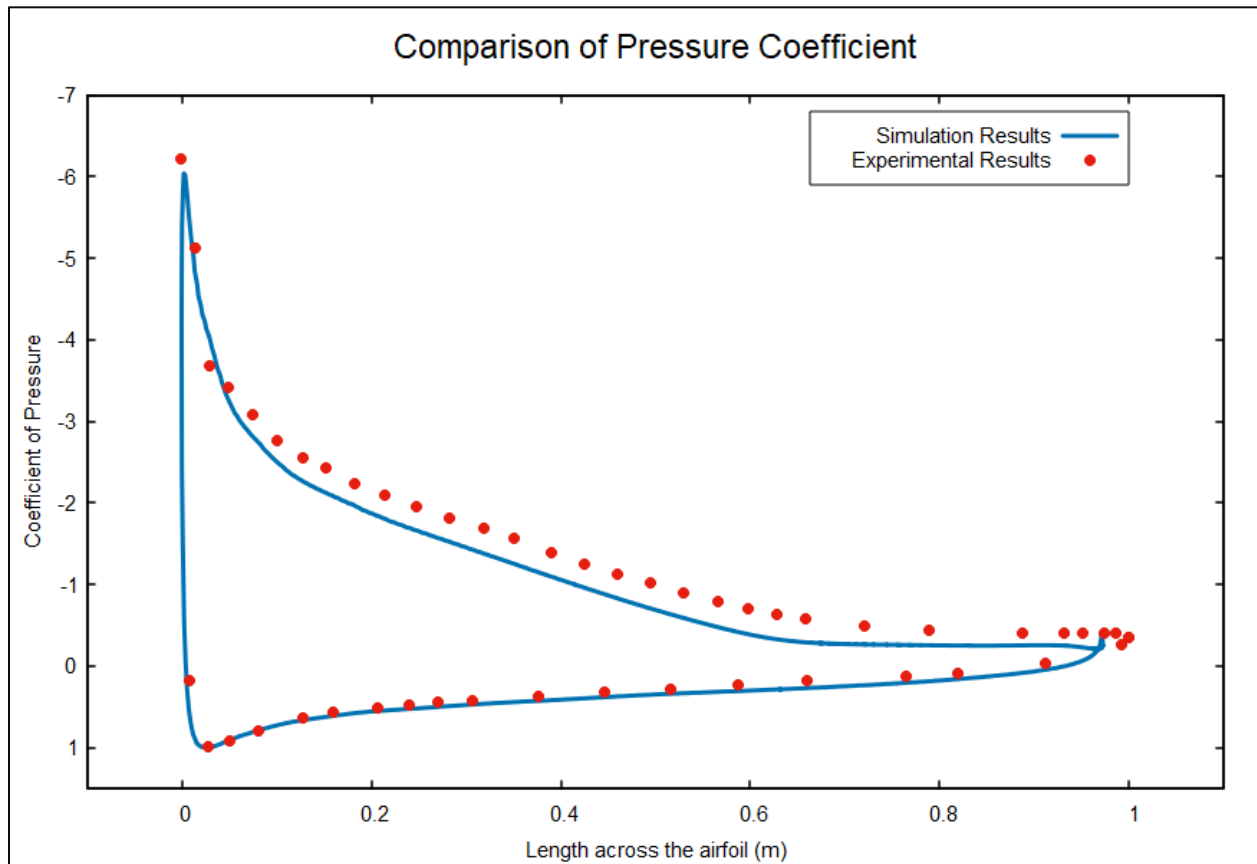

Figure 5.6 Comparison of Pressure Coefficient between Simulation and Experimental results [18].

Table 5.3 shows the comparison of Lift and Drag Coefficients between Experimental [18] and Simulation results. With the y^+ of 0.467, simulation results show good agreement with the experimental results, besides drag due to overestimation of drag coefficient almost double. We will perform grid independence to see any variation in results.

Table 5.3 Comparison of Lift and Drag coefficient with Experimental results [18].

Value	c_l	c_d
Experimental Results	1.7210,1.7170	0.0286,0.0259
Simulation Results	1.459	0.0478
Error [%]	15%, 15.3%	103%, 124%

5.2.7 Grid Independence Study

Grid independence can help get the best optimal grid that negatively alters the results, providing computational efficiency. Two additional grids are created for that purpose, one the coarser than the initial and the other refined. Then the variation of results is monitored, and the most optimal is selected. For the grid variation, the refinement level was altered. Furthermore, a different value of y^+ was chosen to get different near-wall surface layer spacing. For rating, we will check the number of cells, computational time, and results from variations. Table 5.4 shows the results of grid independence.

Table 5.4 Grid Independence study.

Value	Experimental Results	First Gird	Second Grid	Third Grid
Value of y^+	< 1	0.48	0.467	0.3857
First layer Thickness	-	$6.9e-6$	$6.7e-6$	$5.54e-6$
Expansion Ratio	-	1.5	1.3	1.3
Number of Layers	-	10	16	18
Highest Refinement Level	-	7	9	9
Number of Cells	-	43195	53484	55840
c_l	1.7210,1.7170	1.4739	1.4590	1.475
c_d	0.0286,0.0259	0.0507	0.0478	0.046
Computational Time (s)		265	323	335

Looking at the table, all the grids show good results. However, the second grid shows more accuracy to computational time relation. In future, we will be using the second grid as our final grid.

5.3 Simulation of E387 airfoil

The above simulation was performed at a high Reynolds Number, but the out future goal is to study Co-axial propeller at a low Reynolds number and visualize Laminar Separation Bubble. However, in our above studies, we have only performed high Reynolds Number simulations, which leave the validation of Spalart Allmaras to the crucial flaw. Hence, the E387 airfoil, shown in figure 5.7, will be simulated at a different angle of attacks with low Reynolds Number and atmospheric conditions for that purpose. For the velocity, three m/s will be initialized at the inlet to get 200,000 Reynolds Number. For further studies, two different transition models, i.e., KKLOmega and KOmegaSSTLM will be implemented to capture LBM.
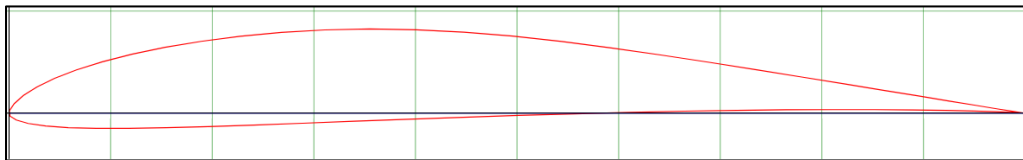

Figure 5.7 E387 airfoil [19] The value of the coefficient of pressures are calculated for 0^0 and $4^0.$

AOA and compared with Experimental results obtained from Morgado et al. studies [10] are shown in figure 5.8 and 5.9, respectively.
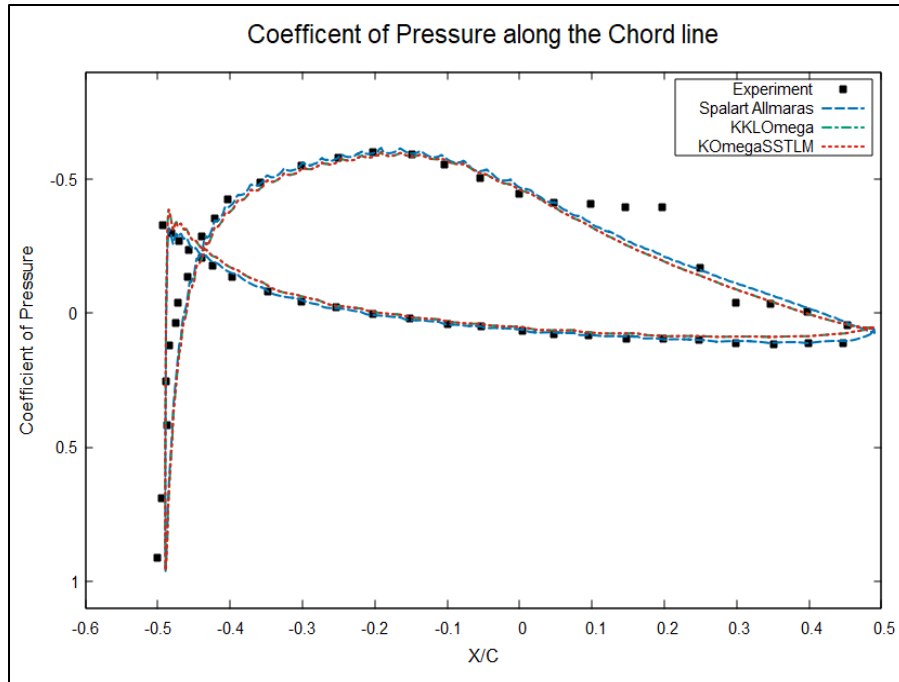
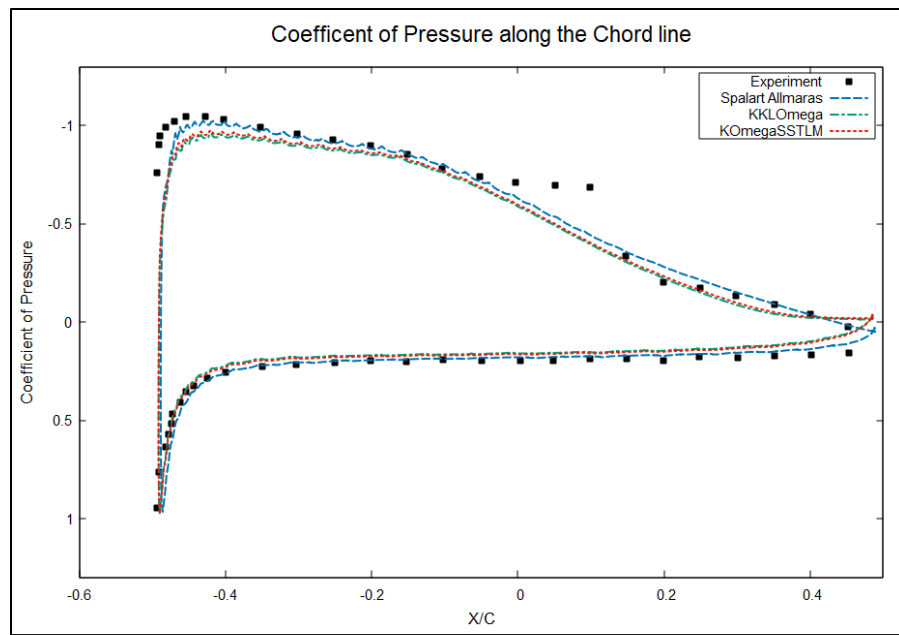Figure 5.8 Simulated Coefficient of Pressure at 0 AOA [10].

Figure 5.9 Simulated Coefficient of Pressure at 4^0 AOA [10].

From the experimental results in 5.8 and 5.9, we can see the Laminar Separation Bubble regime at 0.5 to 0.8 and 0.4 to 0.7, respectively, but Spalart Allmaras and both transition models were unable to capture that phenomenon. Hence the overall lift and drag will be higher than the actual value.
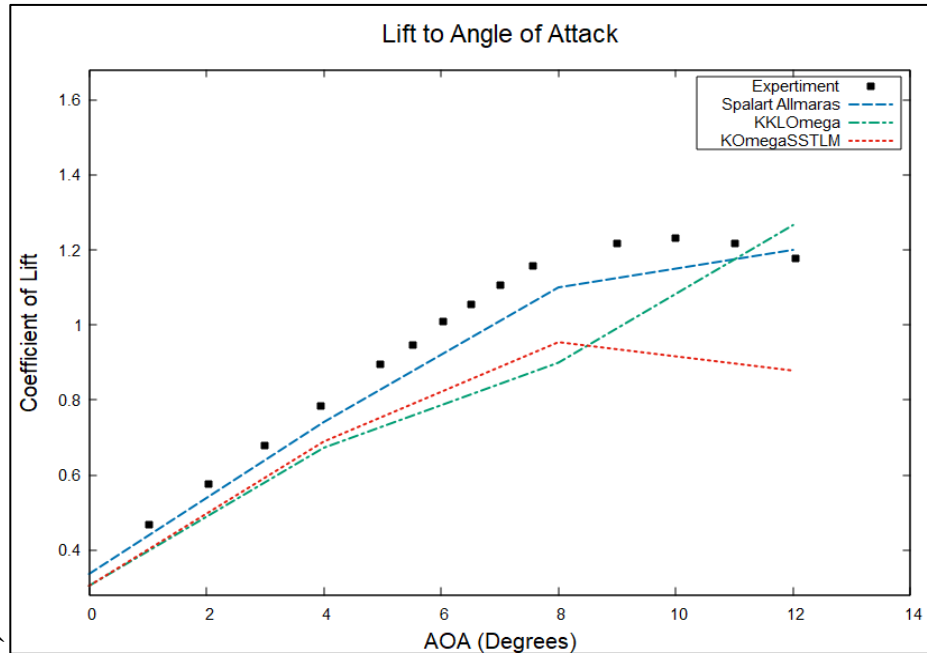

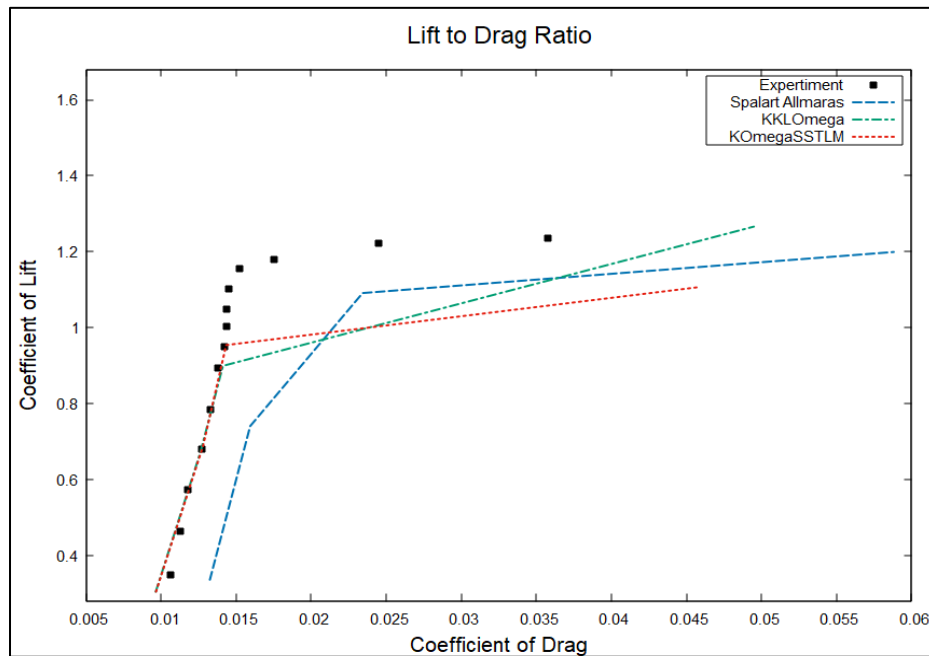Figure 5.10 Coefficient of Lift variation with AOA [10].

Figure 5.11 Coefficient of Lift to Drag Ratio [10].

Comparison of lift and lift to drag ratio between computational and experimental [10] results shown in figure 5.10 and 5.11, respectively, shows that the coefficient of lift obtained from Spalart Allmaras shows good agreement with experimental results. However, the drag is overestimated. The transitional models, though, shows good agreement for the lower angle of attack and started to predict spurious coefficient of lift and drag at a higher angle of attack.

5.4   Discussion

Using the NASA Turbulence Modelling Resource, the simulation was performed to check our case, which will be continued in future. The Spalart Allmaras turbulence model results were compared with the experimental results, and we find reasonably good accuracy. The coefficient of pressure shows accurate results with the experimental results. Then grid independence study was performed to see the variety of results. For which two additional grids were created based on the changing the value of y^+ And refinement level. With the study, we did not find noticeable variation in results. However, results can be improved with the variation of discretization and numerical schemes, but that will be studied in a 3D case where transient dynamic meshing will be performed. Besides that, Spalart Allmaras showed failure in calculating the boundary field around the airfoil, due to which there will be spurious results.

Furthermore, the simulation was performed on a high Reynolds Number that why we were unable to study Laminar Separation Bubble, so for that case, we simulate the E387 airfoil with the best grid from the above grid independence study. Then at a different angle of the attack, say 0, 4, 8 and 12, the simulation was performed at the atmospheric condition with a Reynolds Number of 200,000. Two additional turbulence models KKLOmega and KOmegaSSTLM, were studied, both failed to capture LBM. Also, they showed inaccurate results while calculating the coefficient of lift in comparison with Spalart Allmaras. The results were compared with the study of Morgado, and we found that SA, KKLOmega and KOmegaSSTLM were unable to capture LSB.

6 Simulation of 3D single- and coaxial rotor

This chapter explains the options used while the single and coaxial rotor configurations are being simulated. The verified 2D simulation turbulence model of an airfoil will be used without any changes. During 3D simulation grid production, the same grid measurement technique as the 2D simulation is carried out. The test values from the UiS laboratory shall be utilized for comparison to verify the results of the 3D simulation. The experimental values are collected with the test rig of an RCBenchmark-controlled coaxial rotor thrust stand. RCBenchmark enables the operator to regulate percent change in the throttle and offers torque, thrust, voltage, ampere, engine speed and mechanical power utilization statistics. The test findings were validated using the same propeller and voltage on the test report of the engine supplier. Because the experimental data contains a wide range of RPM values (optical motor speeds), it is easy to compare specific RPM values. In 3D simulations, the RPM value used in the Reynolds number computation and propeller speeds.

6.1 Simulation of Single Rotor

The initial grid and solver setup is as comparable as possible to the 2D validation scenario shown in table 6.1. However, a dynamic mesh requires a comparable but transient solver. In 3D simulations, the pimple is used rather than SIMPLE. The rotation speed as the beginning speed is similar to the rotational speed of the conventional rotor arrangement, which is currently used by Nordic Unmanned when hovering, see Table 4.3. It takes a starting speed of 2000 RPM and a rotating rate of 210 rad/s for AMI to move the propeller.

Table 6.1 Initial Mesh Prams.

Domain size	$25\ m \times 25\ m$
Refinement Level 0 Thickness	$0.26\ m$
Value of y^+	0.4670
First layer Thickness	$6.710e - 6\ m$
Expansion Ratio	1.3
Number of Layers	16
Final Layer Thickness	$2.06e - 5\ m$
Highest Refinement Level on the Wing	9
Highest Refinement level thickness	$9.92e - 7\ m$
Number of Cells	6239534

AMI stands for Arbitrary Mesh Interface and simulates rotating geometry is moving and a stationary component. The AMI should not interfere with the AMI put around the lower propeller in the coaxial setup but be situated around the propeller. A coaxial propeller layout is optimized to operate with pressure and temperature relations under the International Standard Metric Conditions to maximize flight endurance.

6.2 Computational setup

Conduct the same approach as 2D simulations to create Mesh for 3D simulations to determine grid sizes and refinement. The length and width of the domain are 20 times as the propeller radii, y+ < 1, is equal to the thickness of the first layer of $6.7e - 6m$. Implementation grid refining levels and surface layers as shown in figure 6.1 and 6.2. The Torque, as well as the Thrust, converge after 0.1 s. Torque is multiplied by rotational speed [rad/s] to represent the power consumption in [W]. In Table 5.4, three alternative grid refinements can be inspected for the thrust, torque, and power values using the experimental values.
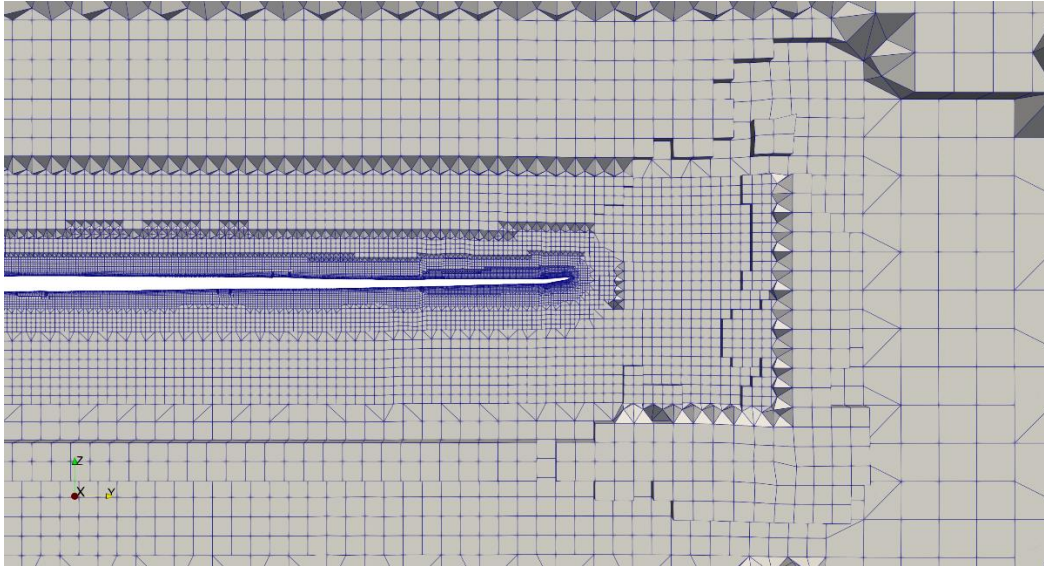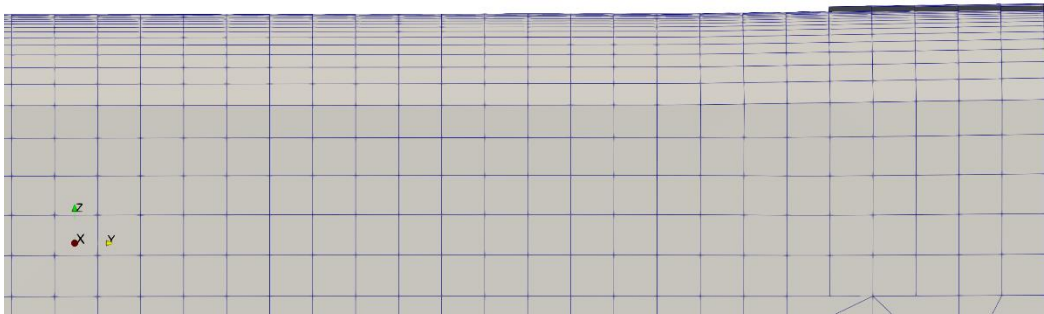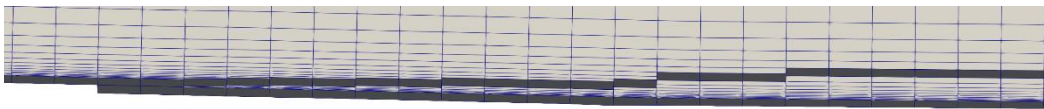
Figure 6.1 Grid Refinement level.

Figure 6.2 Surface layer transition.

In Table 6.1, it is evident that the increase in grid refinement affects the computing time for better y+ and that Thrust, and Torque have negligible alterations. The study of grid refining and independence. The medium grid refining will be employed in the future because there is reasonable y + values in reasonable computing time. The grid adjustments will not make the thrust and torque any benefit. In the following table, the results for a single propeller at 2000 RPM are compared

with experimental results. We can see that the second grid shows reasonable accuracy and grid refinement resulting in optimal computing cost.

Table 6.2 Grid Independence study results for CW propeller at 2000 RPM.

Value	Experimental Results	First Gird	Second Grid	Third Grid
Value of y^+	< 1	0.48	0.467	0.3857
Number of Cells	-	6070546	6239534	7554737
Thrust [N]	35.86	33.2	34.56	34.8
Torque [N-m]	0.85	0.57	0.57	0.58
Power [W]	178.5	119.7	119.7	121.8
Computational Time (s)	-	42582	44100	49741

6.3   RPM range

The simulations are run at different RPM range to check the efficiency of the propeller. For that purpose, 1700, 1850 and 2000 RPM are selected, and the results are as follow.

Table 6.3 Thrust of single propeller at different RPMs.

RPM	1700	1850	2000
Experimental Thrust [N]	26.3	30.3	35.86
Thrust [N]	22.9	32	34.56
Torque [N-m]	0.54	0.7	0.57
Power [W]	113.4	147	119.7
Efficiency [N/W]	0.231	0.217	0.2

Efficiency increased when rotating speed was reduced. The growth ratio between thrust and RPM increases is somewhat below the torque ratio. The differences in the magnitude of the velocity of a domain directly above a single rotor propeller 2000 rpm are presented in Figure 6.3. This means that there is an enhanced blade interference by the higher rotating speed. This decreases the relative

rotary speed in the rotary plane while the influx increase is stable. Reduce thrust potential while preserving torque growth when the rotational speed is increased.
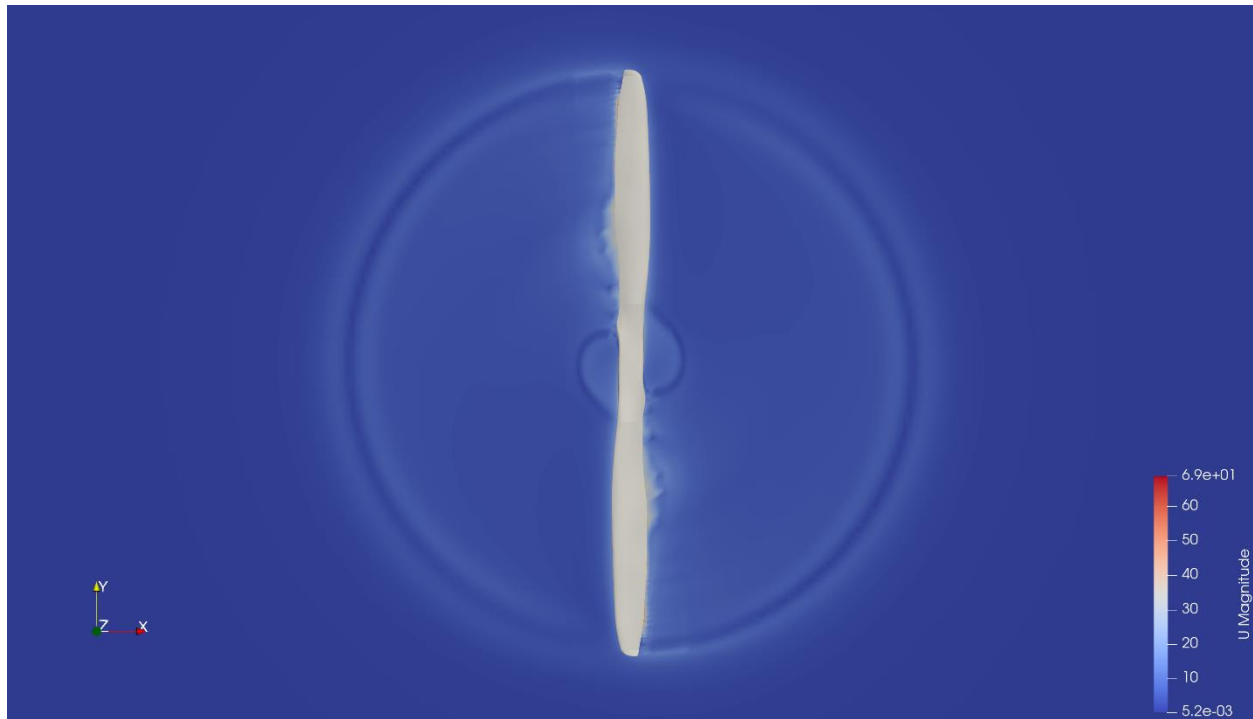

Figure 6.3 Velocity profile at 2000RPM.

6.4   Co-axial Rotor simulation

The propeller 28U 28L configuration will be used at 2000 RPM with different axial separation to mitigate the thrust and efficiency loss. Furthermore, the effect on flight endurance will also be studied in the following section.

6.5   Compotation setup

The computer setup of 3D single and 3D coaxial simulations does not differ a great deal. An extra AMI was added around the lower propeller, precisely the size of the AMI of the upper- and single-rotor propeller, which rotates CCW rather than CW, to produce a counter-rotating coaxial rotating rotor system. As the AMI is a replica of the AMI utilized in the single rotor configuration, no further grid independence analysis will be carried out in the coaxial rotor configuration. Figure 6.5 and 6.6 shows the finished grid of the coaxial rotor arrangement, also on the airfoil.
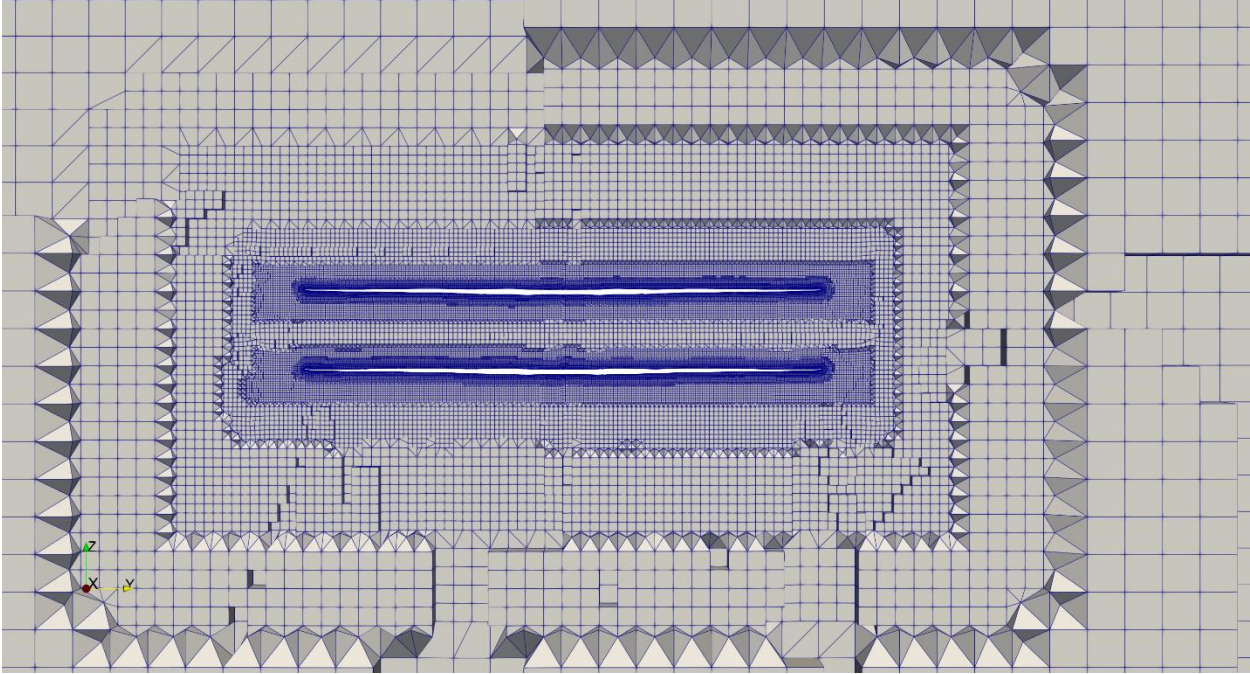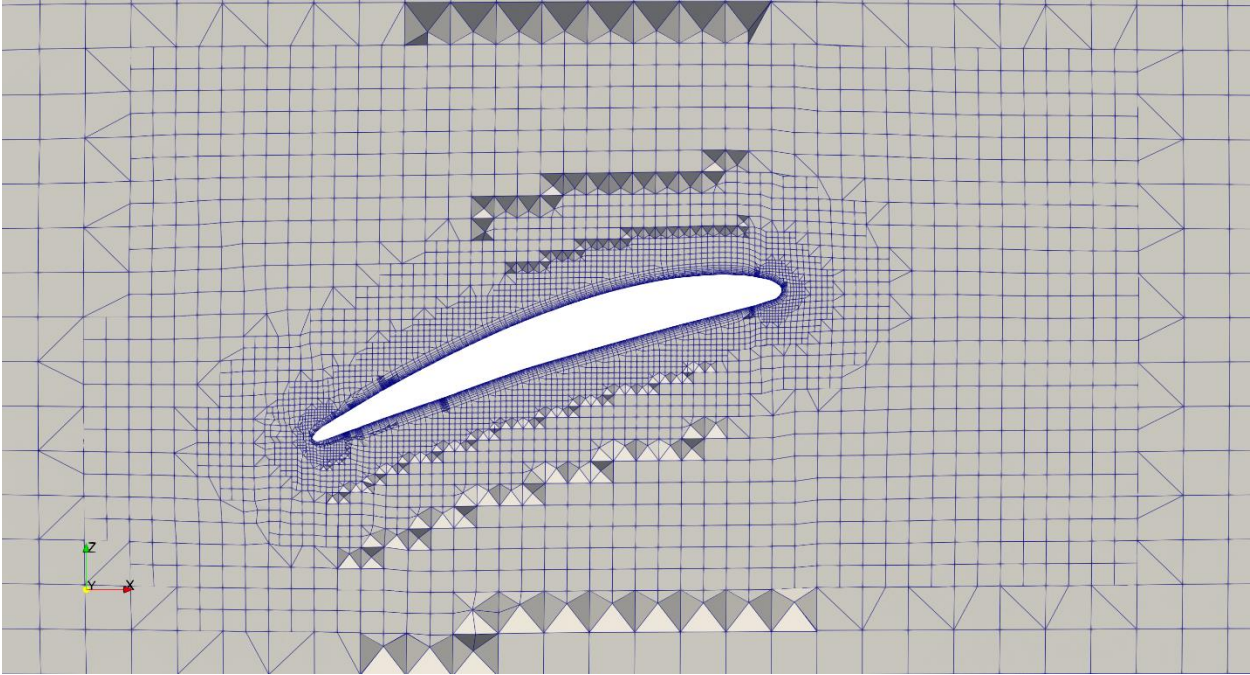
Figure 6.4 Refinement Level.

Figure 6.5 Refinement level over the airfoil.

6.6 Results

Each coaxial rotor simulation result is documented in this subsection. The same thrust is displayed directly in the coaxial result compared to the single rotor result. The axial separation of the coaxial simulation includes data on both the top and lower propellers from a coaxial rotor arrangement with 28U 28L. The axial separation z/R, where z is axial separation length, and R is the radius of rotor, is 0.14z/R, 0.31z/R, 0.36z/R, 0.48z/R, 0.65z/R are used, and the results are mentioned in figure 6.4,

Table 6.4 Coaxial rotor comparison with Axial Separation.

z/R	0.14	0.31	0.36	0.48	0.65
Axial Separation Length [mm]	50	109	127	169	230
Thrust [N]					
Upper propeller	12.32	13.3	13.02	13.16	13.3
Lower propeller	7.94	8.3	9.43	8.47	9.23
Combined	20.26	21.6	22.45	21.63	22.53
Torque [N-m]					
Upper propeller	0.962	1.03	1.014	1.01	1.01
Lower propeller	0.964	0.99	1	0.97	1
Power [W]					
Upper Propeller	202	216.3	212.94	212.4	212.1
Lower Propeller	202.44	207.9	210	203.7	210
Combined	404.46	424.2	420.94	415.7	422.1
Efficiency [N/W]					
Upper Propeller	0.06	0.061	0.061	0.062	0.062
Lower Propeller	0.039	0.04	0.044	0.041	0.044
Combined	0.096	0.101	0.105	0.103	0.107
Experimental	0.089	0.092	0.0918	0.0925	0.093
$\% \, error$	7.86	9.78	14.3	11.3	15

From the comparison of experimental results achieved form the bachelor's students, it shows good agreement with simulation results. Here from the above results, it is clear that as the axial separation increases, the interference of the lower propeller on the upper propeller decreases, resulting in the efficiency increase of the upper propeller. However, due to an increase in axial separation, the lower propeller starts to confront downwash created from the upper propeller results in a decrease in lower propeller efficiency, which in overall efficiency does not increase besides, it decreases. However, at the optimal axial separation, say 0.65z/R gives the highest efficiency. The interference of the lower propeller does not mitigate the efficiency, and the downwash effect is minimal on the lower propeller. This study also follows the trend studied by Brazinkas et al., where he studied the coaxial setup of T-Motor P16"x5.2" propeller.

6.7 Flight Endurance

Unmanned Nordic uses the coaxial configuration for their octocopter, and to increase their flight endurance, we will look into the benefits of increasing the axial separation. A simplified measure of gains in-flight endurance is mentioned below,

$$Flight\ Endurance_{actual} \frac{Combined\ Efficiency_p}{Combined\ Efficiency_s} = Flight\ Endurace_{updated}$$

For axial separation between 0.14 and 0.31 z/R, we have

$$60\ min \frac{0.101}{0.096} = 63.12\ min$$

For axial separation between 0.14 and 0.36 z/R, we have

$$60\ min \frac{0.105}{0.096} = 65.6\ min$$

For axial separation between 0.14 and 0.48 z/R, we have

$$60\ min \frac{0.103}{0.096} = 64.3\ min$$

For axial separation between 0.14 and 0.65 z/R, we have

$$60\ min \frac{0.107}{0.096} = 66.8\ min$$

Hence, from the above practice, it has been clear that due to low interference between upper and lower propeller. Axial separation of 0.65 z/R gives the maximum increase in flight endurance.

7 Conclusion

In this work, five different propellers axial separation distances have been conducted in a coaxial propeller optimization study. 2-dimensional simulation of the airfoil, 3-dimensional single rotor and coaxial rotor simulation were also conducted. The 2-dimensional airfoil simulation was used to validate the 3-dimensional model of turbulence and grid independence investigation.

In order to assess the efficiency of the propeller independently, 3D simulation of a single rotor case has been conducted at different RPM. In order to test propeller combination efficiency, only the most efficient propeller was compared with the standard setup. Each propeller axial separation was simulated to find the most efficient configuration.

By varying the RPM, it has been found that the lowest RPM has the highest efficiency, but the thrust is relatively low. Hence, coaxial simulations were run at 2000 RPM to get the desired thrust too. Firstly, the upper propeller performs poorly due to interference disturbance created by the lower propeller, but as the separation increases, its effect mitigates. However, the lower propeller comes in the region of the slipstream, which causes a loss of efficiency of the lower propeller. Then an optimal separation was selected 0.65 z/R, which has the highest efficiency and gives better flight endurance.

7.1 Future work

In this research, we covered the essential points. We could introduce more propellers and study their effects on efficiency and flight endurance. Then their different combination would have simulated, and the best one would be selected. The basis on that coaxial different coaxial separation distances would have studied to obtain the optimal separation. Then we can move to simulate all four coaxial configurations simultaneously, which will result in more realistic results.

To evaluate and improve simulation inaccuracies, all 3D models should be checked with CMM. All 3D models are also infinitely rigid and can deliver more realistic elastic effects. Secondly, the simulation files should be recreated, and more exact discretization schemes should be adopted, although the surface layer around the tips remains stable and thoroughly developed.

8 References

[1] " www.economist.com.," Taking flight, [Online]. Available: http://www.economist.com/technology-quarterly/2017-06-08/civilian-drones. [Accessed 1 june 2021].

[2] "nordic unmanned," Nordic Unmanned - One of the leading drone service provider in Europe, [Online]. Available: https://nordicunmanned.com/about/. [Accessed 1 June 2021].

[3] S. P. a. J. S. M. Brazinskas, "An Empirical Study of Overlapping Rotor Interference for a Small Unmanned Aircraft Propulsion System,," *Aerospace,* vol. III, no. Oct. 2016., p. p. 32, 2016.

[4] S. D. Prior, "Reviewing and Investigating the Use of Co-Axial Rotor Systems in Small UAVs," *International Journal of Micro Air Vehicles,* vol. 2, no. 1, pp. 1-16, 2010.

[5] "UNIVERSIDADE TECNOL´OGICA FEDERAL DO ... - UTFPR," [Online]. Available: http://repositorio.roca.utfpr.edu.br/jspui/bitstream/1/11813/1/CT_DAMEC_2018_2_44.pdf. [Accessed 1 June 2021].

[6] "https://physics.stackexchange.com/," [Online]. Available: https://physics.stackexchange.com/questions/83432/difference-resultant-aerodynamics-force-on-an-airfoil-and-a-flat-plate. [Accessed 1 june 2021].

[7] empoweringpumps, "THEORY BITES: REYNOLDS NUMBER (CRITERION)," [Online]. Available: https://empoweringpumps.com/theory-bites-reynolds-number-criterion/. [Accessed 17 May 2021].

[8] "Qoura," [Online]. Available: https://www.quora.com/Could-you-explain-the-mechanism-of-the-formation-of-the-boundary-layer-in-a-fluid-flowing-over-a-flat-plate. [Accessed 1 June 2021].

[9] "thefreedictionary.com," [Online]. Available: https://encyclopedia2.thefreedictionary.com/Separation+of+Flow. [Accessed 1 june 2021].

[10] R. V. M. S. J. P. J. Morgado, "XFOIL vs CFD performance predictions for high lift low Reynolds number airfoils,," *Aerospace Science and Technology,* vol. 52, pp. 207-214, 2016.

[11] C. Online, "Introduction to numerical methods," CFD Online, [Online]. Available: https://www.cfd-online.com/Wiki/Introduction_to_numerical_methods. [Accessed 04 April 2021].

[12] [Online]. Available: http://citeseerx.ist.psu.edu/viewdoc/download?doi=10.1.1.524.9868&rep=rep1&type=pdf. [Accessed 09 August 2020].

[13] uis.brage.unit.no, [Online]. Available: https://uis.brage.unit.no/uis-xmlui/bitstream/handle/11250/2458384/PappasZountouridis_Konstantinos.pdf?sequence=2&isAllowed=y. [Accessed 9 August 2020].

[14] S. R. A. P. R. Spalart, "A one-equation turbulence model for aerodynamic flows," *30th Aerospace Sciences Meeting and Exhibit AIAA,* vol. 30th Aerospace Sciences Meeting and Exhibit, Aug 2012.

[15] C. M. R. d. Oliveira, "researchgate," [Online]. Available: https://www.researchgate.net/figure/Figure-B2-Initial-directory-structure-of-each-of-our-OpenFOAM-cases_fig44_317371065. [Accessed 17 May 2021].

[16] N. Unmanned, "STAAKER BG200 - Nordicunmanned - Leading European Provider,," Nordic Unmanned, [Online]. Available: https://nordicunmanned.com/products/unmanned-systems-drones/staaker-bg200/. [Accessed 1 june 2021].

[17] "www.researchgate.net," [Online]. Available: https://www.researchgate.net/figure/Staaker-BG200-multirotor-drone-from-Nordic-Unmanned-and-an-Aerostak-fuel-cell-from-HES_fig1_343589949. [Accessed 1 June 2021].

[18] NASA, "Turbulence Modeling Resource," NASA, [Online]. Available: https://turbmodels.larc.nasa.gov/NACA4412sep_validation/naca4412.cp.expt.dat. [Accessed 02 March 2021].

[19] A. Tools, "Airfoil plotter (e387-il)," Airfoil Tools, [Online]. Available: http://airfoiltools.com/plotter/index?airfoil=e387-il. [Accessed 02 March 2021].

[20] "NACA 4412 (naca4412-il)," Airfoil Tools, [Online]. Available: http://airfoiltools.com/airfoil/details?airfoil=naca4412-il. [Accessed 1 June 2021].